Online Identification of Abdominal Tissues During Grasping Using an Instrumented Laparoscopic Grasper

A THESIS
SUBMITTED TO THE FACULTY OF THE GRADUATE SCHOOL
OF THE UNIVERSITY OF MINNESOTA
BY

Astrini Sie

IN PARTIAL FULFILLMENT OF THE REQUIREMENTS
FOR THE DEGREE OF
MASTER OF SCIENCE

TIMOTHY M. KOWALEWSKI, PhD

August, 2013

© Astrini Sie 2013
ALL RIGHTS RESERVED

Acknowledgements

There are many people who have contributed directly and indirectly to my wonderful experience in graduate school. First and foremost, I would like to express my gratitude for Professor Timothy Kowalewski for his continuous advice, support, trust, and inspiration throughout my master's degree. I would also like to thank Professor Susan Mantell for being a great mentor.

I would like to thank Adhika Lie for every single motivation, conversation, and help he has given me prior to and during my studies in Minnesota. I would like to express my appreciation to my fellow lab members at the Medical Robotics and Devices Lab for the laughters and happenings in the lab: Cory, Jalal, John, Rod, Sachin, and especially Michael Winek for his help on my project.

I would like to acknowledge Tinen Iles and the Visible Heart Laboratory for their help and time related to this project.

Lastly, I would like to thank my parents, to whom I owe my existence and without whom my education would not be possible.

Dedication

To the future generations to come

Abstract

Modern surgical tools provide no advanced features like automated error avoidance or diagnostic information regarding the tissues they interact with. This work motivates and presents the design of a "smart" laparoscopic surgical grasper that can identify the tissue it is grasping while the grasp is occurring. This allows automated prevention of certain errors like crush injury. A nonlinear dynamical model of tissue mechanics is adopted along with an extended Kalman filter to demonstrate the feasibility of this design in simulation and *in situ* and *in vivo* on porcine models. Results indicate that while the approach is sensitive to initial conditions, tissue can be identified during the first 0.3s of a grasp.

Contents

Acknowledgements **i**

Dedication **ii**

Abstract **iii**

List of Tables **vii**

List of Figures **ix**

1 Introduction **1**

1.1 Motivation 1

1.2 Objectives and Scope 3

1.3 State of the Art and Prior Work 3

1.3.1 Instrumented Surgical Graspers 3

1.3.2 Mathematical Models of Tissue 5

1.3.3 Tissue Parameter Estimation 8

1.4 Organization 9

2 Quantifying Force at the Proximal and Distal Ends of a Laparoscopic Surgical Grasper **10**

2.1 Experimental Force Quantification at Grasper Handle and Jaws 11

2.1.1 Experimental Protocol 11

2.1.2 Results and Interpretation 13

2.1.3 Interpretation and Conclusion 13

2.2 Alternative Methods for Direct Force Quantification at Grasper Jaws . . 16
2.2.1 Pressure Indication Microcapsules Sheet 16
2.3 Conclusion 20

3 Hardware and Software Development 21
3.1 The Mechanical Smart Endoscopic Grasper 21
3.1.1 MSEG Kinematic Mechanism 21
3.1.2 MSEG Sensors and Actuators 22
3.1.3 MSEG Software and Graphical User Interface 23
3.2 The *Smart Tool* - Modifications of the Mechanical Smart Endoscopic Grasper 23
3.2.1 MSEG Hardware Modifications 24
3.2.2 MSEG Software and Hardware-Software Interface Modifications . 25
3.3 MSEG Calibration 29
3.3.1 Motor Command to Motor Force Relationship 29
3.3.2 Force Calibration 30
3.3.3 Displacement Calibration 36
3.3.4 Filtering of Raw Data 40
3.3.5 Summary of Calibration 40

4 Development of an Extended Kalman Filter for Online Tissue Identification 42
4.1 The Extended Kalman Filter 43
4.1.1 Time / System Model 43
4.1.2 Measurement Model 46
4.2 Verification of the Extended Kalman Filter for Simulation of Tissue Model during Grasping 47
4.2.1 Simulation of Tissue Model during Grasping 47
4.2.2 EKF Tuning and Results 50
4.2.3 Discussion and Conclusion 51
4.3 Identification of Tissue Simulation Using Extended Kalman Filter . . . 54
4.3.1 EKF Tuning and Results 54
4.3.2 Discussion and Conclusion 55

4.4 The Recursive Least Squares Estimator 57
4.4.1 RLS Estimator Tuning and Results 60
4.4.2 Discussion and Conclusion 61

5 Identification of *In Vivo* and *In Situ* Porcine Tissues Using Extended Kalman Filter 65
5.1 Pre-Experimental Protocol and Setup 65
5.1.1 Setting Input Voltage to Motor 65
5.1.2 Test Grasping on Hand Tissue 67
5.2 Experimental Protocol and Setup 67
5.2.1 Data Collection on Porcine Models 67
5.2.2 Analysis of Raw Data 70
5.3 EKF Implementation and Results 71
5.4 Discussion and Conclusion 73
5.5 RLS Implementation, Results, and Conclusion 75

6 Conclusion and Future Work 84
6.1 Conclusion 84
6.2 Future Work 85

References 87

Appendix A. Glossary and Acronyms 93
A.1 Glossary 93
A.2 Acronyms 94
A.3 *LabVIEW* Block Diagram of *Smart Tool* GUI 95

List of Tables

2.1 Normalized Mean Intensity and Calculated Area of Colored Pixels for Calibration and Pressure Indication Experiment with Fixed Weight and MSEG 18
3.1 The Measured Values of All Grasper Links Lengths and Other Relevant Grasper Geometry 34
4.1 Parameters Used for Simulation of Nonlinear Model of Soft Tissue During Grasping 48
4.2 Covariance Matrices for EKF Verification Simulation 51
4.3 Steady State Values of Estimated States and Actual States in EKF Verification Simulation 51
4.4 Convergence Time and Value of Force Error of EKF Verification Simulation 53
4.5 Covariance Matrices for Tissue Identification Simulation 57
4.6 Steady State Values of Estimated States and Actual States in Tissue Identification Simulation 57
4.7 Convergence Time and Value of Force Error of Tissue Identification Simulation 58
4.8 Convergence Time and Force Error for Simulation of Tissue Models with Four Different Initial Estimate of Parameters 62
5.1 Tissue Parameters for EKF Implementation on Porcine Tissue Data . . 74
5.2 Tissue Parameters for EKF Implementation on Porcine Tissue Identification 74
5.3 System, Noise, and Measurement Covariance Matrices for EKF Implementation on Porcine Tissue Identification 75
5.4 Convergence Time and Force Error for Porcine Tissues Identification . . 77

5.5 Steady State Values of Estimated States and Actual States for Porcine Tissues Identification 77
A.1 Acronyms 94

List of Figures

1.1 Errors in silicone phantom palpation experiment [1] 5
1.2 Rendered CAD drawing of MEG without protective top cover [2] 6
1.3 Percentage of successful tissue characterizations for surgeons and non-surgeons using direct exploration (DE), visual (V) and force (F) feedback [3] 6
1.4 Stress strain curves for liver (LV), large intestine (LI), stomach (ST), small intestine (SI), spleen (SP), gallbladder (GB), and bladder (BL) after one (1) and five (5) tissue loading cycles [4] 7
2.1 Setup for MSEG force quantification experiments 12
2.2 Setup for EDGE force quantification experiments 12
2.3 Box plot of applied weights at handle (proximal end) vs measured strain values for the MSEG 13
2.4 Box plot of applied weights at grasper jaws (distal end) vs measured strain values for the MSEG 14
2.5 Measured force values vs jaw angle at different applied weight intervals over full swipe handle position for the EDGE grasper 15
2.6 Setup for pressure indication experiments on phantom bowel tissue . . . 17
2.7 Pressure gradient colormap for pressure indicator sheet experiments . . 19
3.1 (a) CAD Drawing of the MSEG (b) close up view of the Babcock grasper (c) Driving mechanism of the MSEG [5] 22
3.2 Close up view of the MSEG sensor head [6] 23
3.3 Screen capture of Roan's original MSEG GUI with (clockwise from top) temperature chart, jaw displacement chart, grasp force chart, optical absorption chart, and impedance chart [6] 24

3.4 Touch sensors configuration 25
3.5 Pinout of PCI6230 26
3.6 Photo of connection to PCI6230 board 27
3.7 Cable connection from PCI6230 board with numbers adjacent to cables indicating respective PCI6230 pin number connected 27
3.8 Front panel of *Smart Tool* GUI in *LabVIEW* 28
3.9 Box plot of input command to motor versus output voltage from strain gage 30
3.10 Plot of input command to motor versus output voltage median from strain gage together with the fitted curve 31
3.11 Plot of strain gage voltage versus applied weights at partial pulley (handle) 32
3.12 Free body diagram of the partial pulley (handle) and pushrod 33
3.13 Free body digaram of grasper jaw connected to pushrod via scissor linkage mechanism 34
3.14 Free body diagrams for grasper jaw and pins 35
3.15 Setup of Force Calibration Verification 36
3.16 Plot of Scale Reading versus Strain Gage Reading 36
3.17 The gage block and cylindrical weight piece used for the force correction experiment 37
3.18 Plot of strain gage voltage versus encoder angle for all three jaw separation distances together with the fitted line used to derive the force correction factor for angle measurements 38
3.19 Linkage geometry of grasper jaws and scissor linkage mechanism drawn while fully closed and open 39
3.20 Flowchart of calibration process from raw strain gage and encoder data to force and displacement at tissue 41
4.1 *SIMULINK* block diagram of nonlinear model for tissue during grasping 48
4.2 Input force for simulation of nonlinear tissue model in *SIMULINK* . . . 49
4.3 Resulting tissue displacements obtained from simulation of nonlinear tissue in *SIMULINK* 50
4.4 Liver simulation results 52
4.5 Small bowel simulation results 53

4.6 Bladder simulation results 54
4.7 Gallbladder simulation results 55
4.8 Stress-strain plots for various tissue types using $\hat{\alpha}$ and $\hat{\beta}$ estimated from EKF simulation 56
4.9 Stress-strain plots for various tissue types using four different initial guess tissue 59
4.10 Plots of the actual and estimated force-displacement curve and α, β for liver 63
4.11 Plots of the actual and estimated force-displacement curve and α, β for small bowel 63
4.12 Plots of the actual and estimated force-displacement curve for bladder . 64
4.13 Plots of the actual and estimated force-displacement curve and α, β for gallbladder 64
5.1 Trapezoidal voltage profile output to the motor at 0.25Hz (left), 2Hz (middle), and 4Hz (right) frequencies 66
5.2 Sensor outputs and motor command for hand tissue grasping 68
5.3 Abdomen of pig that has been cut open 69
5.4 Setup of a grasping session 70
5.5 Grasping session performed on *in situ* organs 71
5.6 Raw sensor outputs and motor command for one porcine tissue grasping session 72
5.7 Calibrated force delivered to the tissue, tissue displacement, and initial thickness plots for one single grasp 73
5.8 Estimated and actual states for 0.25Hz, 2V (1.55N) single grasp on liver tissue 76
5.9 Estimated and actual force, force error and error threshold for 0.25Hz, 2V (1.55N) single grasp on liver tissue 77
5.10 Plot of steady state values of estimated $\hat{\bar{\alpha}}$ and boxplot for all grasps on all four tissue types 78
5.11 Plot of steady state values of estimated $\hat{\bar{\beta}}$ and boxplot for all grasps on all four tissue types 78

5.12 Plot of steady state values of estimated $\hat{d}$ and boxplot for all grasps on all four tissue types 79
5.13 *MATLAB* multicomparison results of $\hat{\bar{\alpha}}$ 80
5.14 *MATLAB* multicomparison results of $\hat{\bar{\beta}}$ 81
5.15 *MATLAB* multicomparison results of $\hat{d}$ 82
5.16 Plots of the actual and estimated force-displacement curve for 0.25Hz, 2V (1.55N) single grasp on liver tissue 83
A.1 Block diagram of *Smart Tool* GUI in *LabVIEW* 95

Chapter 1

Introduction

1.1 Motivation

In recent years, surgical procedures in the abdominal cavity have been migrating from open surgery to minimally invasive surgery (MIS) [7]. MIS in the abdominal organs is referred to as laparoscopic surgery. Improvements of technology in MIS provides benefits to patients compared to traditional open surgeries such as reduced blood loss, improved cosmetics due to smaller incisions [1], and also faster recovery times and shorter hospitalization periods [8, 9, 10]. Nevertheless, despite the general improvements that MIS brings to patients, from the surgeons' point of view, MIS introduces an additional tool that interfaces the actuation from the surgeon's hand to the patient's tissue, thus eliminating direct contact between the two. Without direct contact with tissue, surgeons lose their sense of touch (tactile feedback) and force (haptic feedback) from the tissue. Such absence may result in the inability to avoid tissue injuries or "feel out" different tissue types or conditions. Clinicians may thus exert unintentional excessive forces on tissue and so increase the chances of tissue-related injuries that cause adverse effects to patients.

In [11], De observes that grasper induced tissue injuries from improper tissue handling may lead to ileus, scar formation, bleeding, and adhesions [12, 13, 14]. Moreover, organs such as liver, small bowel, and ureter might be subjected to more severe injuries such as perforation or hemorrhage [15, 16]. Perforation in gallbladder occurs in 15 out of 20 laparoscopic procedures [7]. Prolonged tissue grasping with excessive forces

might also lead to tissue ischemia, where the blood level of tissue drops below normal, causing oxygen deprivation and build up of metabolic waste. The study performed in [17] found that inappropriate use of force doubles the risk of bile, vascular, and bowel complications in laparoscopic cholecystectomy. [7]

While information of the actual force delivered to the tissue at the grasper jaws is important, current MIS surgical evaluation or training platforms such as FLS [18], ICSAD [19], and ADEPT [20] provide no information on the force values. Meanwhile, being aware of the adverse effect an absence of force feedback can produce, prior work designed "atraumatic" graspers to minimize tissue ischemia by pure mechanical means [21, 22, 23, 24, 25, 26] or instrumented tools that assist surgeons in detecting tissue ischemia [27, 28, 6]. While these tools presented means to prevent tissue ischemia by reducing grasping pressure and quantifying force exerted by surgeon, they fail to address the variety of grasping scenarios for various tissues, and that different tissues have varying limits of maximum force threshold.

This gap motivates an instrumented tool that is capable of differentiating tissues in real time and to subsequently apply a dedicated control algorithm based on the tissue parameters to regulate actual force delivered to the tissue. Although such a tool will not recover tactile and haptic feedback to surgeons, the tool is able to mitigate problems caused by the lack of tactile and haptic feedback including automated minimization of tissue injuries and thus result in a safer MIS procedure for both surgeons and patients.

In [29], it is mentioned that applying too little force to the tissue is inefficient, while applying to much force to the tissue causes tissue injuries. As different tissues have different "optimal" force values and "maximum" force limits, we have to first identify the tissue types being handled, and only then set the force delivered to the tissue according the corresponding tissue's optimal value. Thus, prior to being able to regulate force delivered to the tissue, the aforementioned tool has to be able to perform tissue differentiation. The primary motivation of this work is to equip a laparoscopic grasper with the ability to perform such tissue identification in real time in order to enable safe, automated, tissue-specific handling in surgery.

If successful, this work can be implemented in existing MIS systems - particularly surgical robotics - to set tissue-specific control loop parameters in real time. Most notably, tissue-specific force thresholds can be set for each grasp to avoid tissue injury

by excessive force yet simultaneously avoid loss of traction through insufficient force.

1.2 Objectives and Scope

The main objective of this work is to develop a smart instrumented laparoscopic grasper for applications in MIS and/or robotic surgery that is able to perform the following tasks:

- Quantify the force delivered to tissue at the tool-tip interface or grasper jaws (distal end) given a force exerted by surgeon or robot actuator at the handle (proximal end).
- Perform online tissue identification *in vivo* or *in situ* by differentiating typical tissue types handled in laparoscopic procedure via mechanical properties and a dynamic tissue model.

The scope of this work is limited to minimal hardware modification of an existing laparascopic grasper, and is focused on system identification via online parameter estimation algorithm development and verification in simulation, followed by application in the aforementioned grasper and experimental testing on *in vivo* and *in situ* tissue models.

For the context of this work, the instrumented laparoscopic grasper will be referred to as the *Smart Tool* throughout this document.

1.3 State of the Art and Prior Work

1.3.1 Instrumented Surgical Graspers

Over the past two decades, various surgical graspers capable of detecting tissue ischemia have been designed. Moreover, some works claimed to have developed graspers that can restore surgeon's haptic perception by providing force feedback.

In [30], the authors developed a sensor that detects ischemic tissue based on change in electrical impedance. Then, motivated with the need to increase surgeons sensing capabilities, Fischer et al. developed an ischemia and force sensing surgical instruments in [28, 27]. The tool developed uses two bi-color LEDs and a photodiode to measure

oxygen saturation in tissue to detect tissue ischemia. The force sensor implemented is a foil strain gage in Wheatstone bridge configuration. The sensor data were presented in a graphical user interface (GUI) for surgeon to monitor tissue condition.

In 1999, Rosen et al. [31] and McFarlane et al. [1] proposed a force feedback endoscopic grasper (FREG). Using the grasper, a group of surgeons and nonsurgeons are able to rank the compliance of a silicone phantom during palpation. Nevertheless, as seen in Figure 1.1 the observed error remains higher than direct hand contact although much lower than typical uninstrumented graspers. In 2002, Brown et al. [32] furthered this work by adapting the FREG to a motorized endoscopic grasper (MEG) that uses a brushed DC motor instead of a flat-coil actuator, as shown in Figure 1.2. The MEG developed uses a pair of parallel strain gages at the handle (shaped like a partial pulley) to measure the force exerted by the DC motor (controlled by the surgeon). The DC motor is connected to the partial pulley using a cable, and via typical laparoscopic linkage connections, rotation of partial pulley produces opening and closing motion of the grasper jaws. The MEG was used to detect biomechanical properties (stress-strain) of several abdominal soft tissue under compressive loads *in vivo* and *ex vivo* [2, 4], which indicates a large variation between tissue properties measured *in vivo* and *ex vivo*. Next, Roan et al. [6] furthered the work by improving the MEG into the motorized smart endoscopic grasper (MSEG), a robust data collection platform capable of real-time feedback to make *in vivo* measurements of force, deformation, temperature, optical absorption, and electrical impedance detections of live porcine tissues. Roan's work observed an interesting phenomenon that variation of tissue properties between one porcine model and another can be larger than that of healthy and ischemic tissue on the same porcine model.

In 2005, Tholey et al.[3] developed an instrumented laparoscopic grasper for robotic surgery that combines force and vision feedback. The graspers are actuated by cable-driven pulley mechanism using to the DC motor. In the work, force is measured based on the current that is drawn by the DC motor. Then, this value of force is fedback to the surgeon via the PHANToM platform (Sensable Technologies, Woburn, MA, USA). The tool is able to perform tissue characterization well, and using both force and vision feedback, it is shown in Figure 1.3 that a group of 10 surgeons and 10 non-surgeons demonstrate higher ability to differentiate three artificial tissue types with different

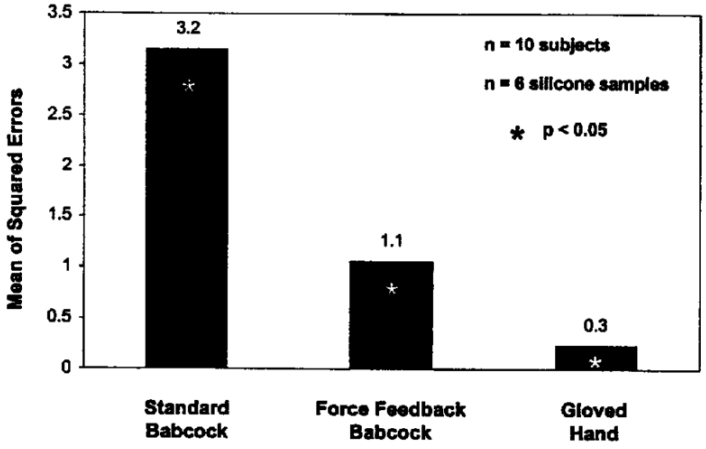

Figure 1.1: Errors in silicone phantom palpation experiment [1]

stiffnesses (soft, medium, and hard).

The existing instrumented laparoscopic graspers are able to detect tissue properties that help surgeons in detecting ischemic tissues. Some of the graspers are capable of performing tissue biomechanical properties characterization and subsequently restore the surgeon's haptic perception by providing a force feedback. Nevertheless, tools that are capable of providing an automatic regulation or control that is tailored to different tissue types have not been developed yet. Even though haptic perception is restored, surgeons might still apply excessive amounts of force to the tissue because of misinterpretation on tissue types. This motivates our work on developing a smart laparoscopic grasper that is able to address such problem and provide and an automated solution.

1.3.2 Mathematical Models of Tissue

The behavior of soft tissue under force application demonstrates nonlinear viscoelastic characteristics [33]. Nevertheless, due to computational complexity of nonlinear tissue models, most existing work assumes a linear tissue model. The most commonly adapted tissue models are the mass-spring-damper model [34, 35] and the Kelvin-Voigt model [36, 37]. Other works have also used nonlinear tissue models such as polynomial models [38, 39] and the Hunt-Crossley model [40, 41]. [42]

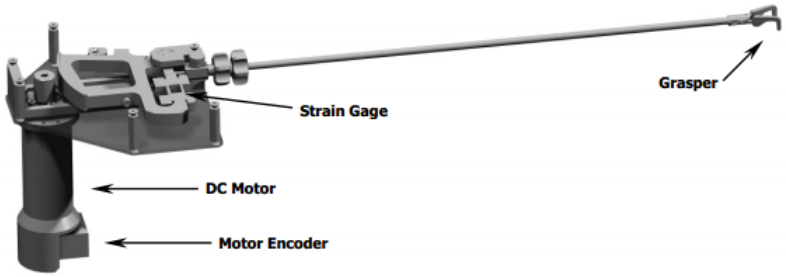

Figure 1.2: Rendered CAD drawing of MEG without protective top cover [2]

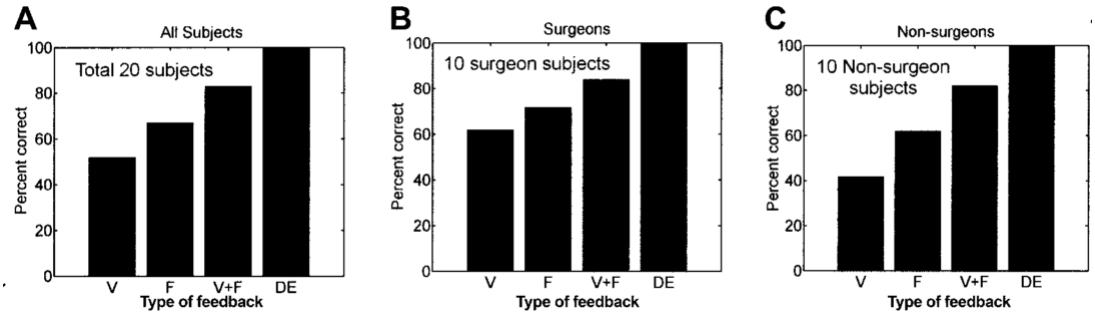

Figure 1.3: Percentage of successful tissue characterizations for surgeons and non-surgeons using direct exploration (DE), visual (V) and force (F) feedback [3]

In [4], Rosen et al. performed extensive biomechanical characterization of seven organs in the abdomen of 14 porcine models. In the work, the authors propose eight elastic models for describing the elastic characteristics of tissue. The models chosen relate stress applied to tissue and the resulting strain produced. Using nonlinear regression, respective tissue parameters are approximated to fit the chosen elastic equations. Figure 1.4 shows the resulting stress strain curves for all seven organs after one and five cycles of loadings based on experimental data collection from the porcine models. Based on the regression, it is found that the exponential function previously used by several researchers in describing tissue elastic models (Equation 1.1) has a marginally poorer fit than two new functions he proposed (Equations 1.2 and 1.3). In the equations, σ is stress applied to tissue, ϵ is resulting tissue strain, and α, β, γ are tissue stiffness

parameters.

$$\sigma = \beta(e^{\alpha\epsilon} - 1) \tag{1.1}$$

$$\sigma = \beta(e^{\alpha\epsilon} - 1) + \gamma\epsilon \tag{1.2}$$

$$\sigma = \beta\left(\frac{1}{1-\alpha\epsilon} - 1\right) \tag{1.3}$$

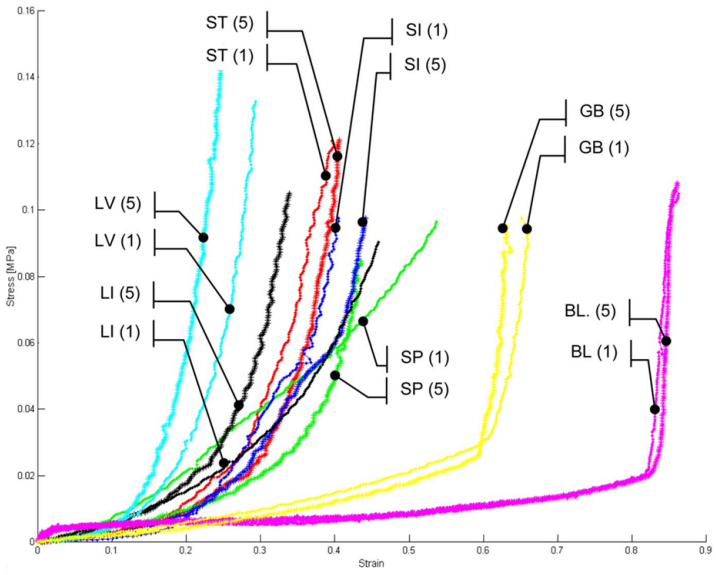

Figure 1.4: Stress strain curves for liver (LV), large intestine (LI), stomach (ST), small intestine (SI), spleen (SP), gallbladder (GB), and bladder (BL) after one (1) and five (5) tissue loading cycles [4]

Most of the existing presented tissue mathematical models involve only terms that describe steady state tissue mechanical behavior, that is relationship between applied force or stress and resulting strain. Nevertheless, these models provide no information on transient tissue behavior. Realistically during the surgery, depending on the grasp and hold period, tissue might never reach a "steady state" or stay in steady state for a very brief period and then transition into another steady state due to fast grasp and release motions. In [43], Yu et al. proposed a nonlinear mass-spring-damper tissue dynamics model as shown in Equation 1.4, in which u is force applied to tissue, x

is tissue displacement, d is tissue damping coefficient, and α, β are tissue stiffness parameters. This model allows for modeling transient behavior, while incorporating empirically verified nonlinear properties.

$$u = m\ddot{x} + d\dot{x} + \alpha(e^{\beta x} - 1) \tag{1.4}$$

1.3.3 Tissue Parameter Estimation

Several existing works have performed parameter estimation for systems with elastic mathematical models. Parameter estimation of the environment during robotic surgery that consists of a master robot and slave robot is performed in [44] using indirect adaptation technique and [41] using self-perturbing recursive least squares (RLS) [45]. The Extended Kalman filter (EKF) algorithm is used in [46] to estimate stiffness parameters of a telesurgery environment online.

In addition to elastic models in general, several works have narrowed down the estimation for tissue-specific models. Nevertheless, these works use artificial tissue surrogates or silicone-based phantom tissue and have not verified the estimation algorithms *in vivo* or *in situ* in animals. In [47], Hoshi et al. developed an extended Kalman filter (EKF) algorithm to estimate tissue parameters by assuming a linear spring model for tissue. The work successfully identified Young's modulus of different artificial tissues using force and displacement data measured in the experiment. In [37] performed extensive analysis by comparing the recursive least square (RLS), adaptive identification (AI), and multi-estimator (ME) algorithms for identifying stiffness parameters of three artifical tissues made from different synthetic materials. The work assumes a linear Kelvin-Voigt tissue model and concludes that RLS and ME algorithms work best for online paramter estimation in this case. Next, in [42], Yamamoto et al. furthered the work by extending the estimation algorithms to seven linear and nonlinear tissue models. The analysis is extended to detecting change in stiffness parameters of an artificial calcified artery (wooden coffee stirrer) that is inserted to the silicone phantom tissue model, but not for discriminating typical abdominal tissues.

In this work, we develop an estimation algorithm that is tested on nonlinear dynamic tissue models in both simulation and on *in vivo* and *in situ* porcine tissue models.

1.4 Organization

- Chapter 1 provides an introduction of this work by elaborating the motivation, goals, and scope. Furthermore, the chapter provides a review of literature review and state of art of MIS, laparoscopic graspers with force feedback, and existing tissue dynamic models.

- Chapter 2 describes the force quantification procedures at the handle and grasper jaws. Also, the chapter briefly discusses alternative methods for force quantification directly at the grasper jaws. This work was published as a stand-alone method for quantifying force exerted by a tool on tissue and its results are not directly used in subsequent chapters.

- Chapter 3 briefly covers the design and general setup of software and hardware that are implemented in this project, as well as calibration of the sensors and actuators.

- Chapter 4 demonstrates the algorithm design for tissue parameters estimation and identification during grasping. In the chapter, the algorithm is tested in simulation by using a nonlinear dynamic tissue model.

- Chapter 5 discusses the application of tissue parameters estimation and identification algorithm on tissue data of *in situ* porcine models.

- Chapter 6 concludes the work with a final discussion and analysis presented in this thesis, and proposes future work to improve the scope and extend the results of this thesis.

Chapter 2

Quantifying Force at the Proximal and Distal Ends of a Laparoscopic Surgical Grasper

In the existing instrumented laparoscopic surgical graspers, sensors are deliberately placed at the proximal end, far away from the grasper jaws [32, 31, 11, 6]. By doing so, minimal modifications have to be performed to existing off-the-shelf grasper jaws [31], and sterility of the contact surface between the jaws and tissue is not an issue. By placing force and displacement sensors far away from the grasper jaws, we have to rely on kinematics to derive the actual force that is delivered to the tissue at the grasper jaws from the measurement of force that is applied by the surgeon at the handle. Such force and displacement kinematic relationships have been derived in several works such as [31, 6] and more thoroughly in Chapter 3. In this chapter, we observe that proximal sensor measurement at the handle introduces unavoidable errors in measuring actual forces at the grasper jaws. This chapter discusses experimental characterization of force and displacement quantification both at the handle and at the grasper jaws. Lastly, an alternative low cost method of quantifying force that is actually delivered to the tissue is proposed.

2.1 Experimental Force Quantification at Grasper Handle and Jaws

In this section (largely based on the work in [48]), we develop a portable, general test bed for measuring the force at the proximal end or handle (the force applied by the surgeon) and directly at the distal end or grasper jaws (the force delivered to the tissue) of a laparoscopic grasper. We experimentally characterize the mappings between proximally measured and distally applied forces for two different laparoscopic tools: the motorized Mechanical Smart Endoscopic Grasper (MSEG) developed by Roan [6] and the Electronic Data Generation and Evaluation (EDGE) system (Simulab Corporation, Seattle, WA).

2.1.1 Experimental Protocol

A calibration test bed was designed and machined. The CAD model was established based on a Babcock grasper (#33510 BL, Karl Storz GmBH & Co. KG, Tuttlingen Germany) used in the MSEG and a Maryland Grasper in the EDGE System. Hanging weights were favored over electromechanical sensors and actuators to lower costs.

We performed experiments on the MSEG. The MSEG was bolted into the test bed and erected on a tripod. The motor was disconnected from the partial pulley, and a 0.024 inch uncoated stainless steel cable (#2024, Sava Industries Inc, Riverdale NJ) was wrapped around the linkage, one end connected to the MSEG partial pulley and another end placed over a ball-bearing pulley, connected to incremental cylinder weights. The experimental setup is shown in Figure 2.1(a).

A graphical user interface (GUI) and additional data acquisition channels were developed based on the original software of Roan et al. and the EDGE system. The experiment was performed by starting data logging then applying incremental cylinder weights to the proximal linkage (handle) of the MSEG. The cylinder weights were added incrementally from 100g to a total of 1,000g with a time delay of 5s for each increment. While the experiment was running, the built-in strain gauges in the proximal end measured the force applied from the weights and the measurement data was recorded in log files as raw internal data.

Once calibrated, the experiment was repeated with applying the same sequence of

weights at the distal end (grasper jaws) of the MSEG. Another calibration test bed was erected on a tripod, supporting the distal end of the MSEG. One jaw was fixed and the other jaw was connected to the weights. The proximal partial pulley position was held constant by a mechanical bolt attached to the calibration test bed. The experimental setup for this experiment is shown in Figure 2.1(b).

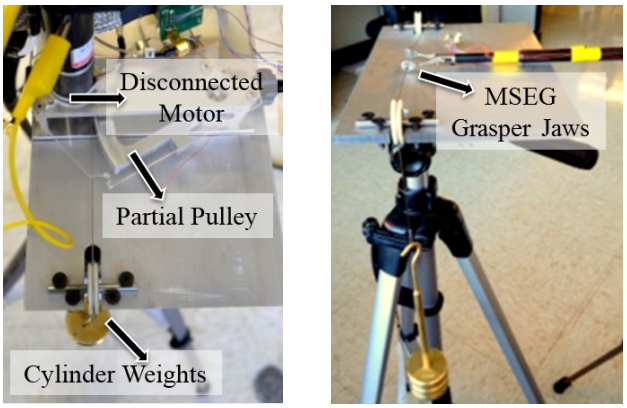

(a) Proximal experiment (b) Distal experiment

Figure 2.1: Setup for MSEG force quantification experiments

In addition to the MSEG, we performed experiments on the EDGE grasper. The setup for this experiment was similar to the experiment at the distal end of the MSEG, except the EDGE grasper was positioned on the EDGE platform, shown in Figure 2.2, and the grasper handle was manually swept through its full range. Measured force and jaw angle data were recorded via the GUI from the EDGE platform.

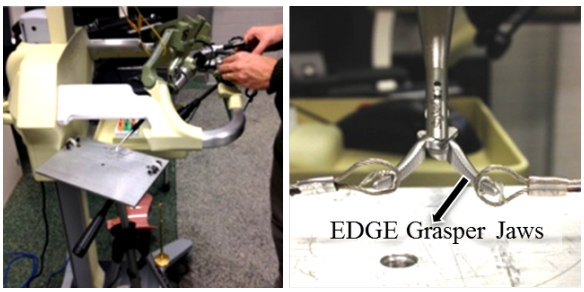

Figure 2.2: Setup for EDGE force quantification experiments

2.1.2 Results and Interpretation

The plot of strain gage measurement versus the applied weights for the MSEG handle is shown in Figure 2.3, while Figure 2.4 shows the plot of strain values versus applied weight for the experiment at the MSEG tool tip.

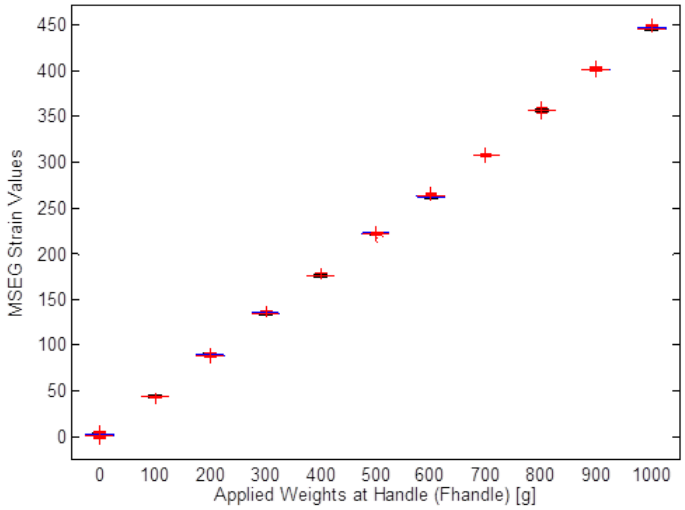

Figure 2.3: Box plot of applied weights at handle (proximal end) vs measured strain values for the MSEG

Figure 2.5(a) shows the plot of measured force (F_{meas}) by EDGE sensors versus jaw angle for each applied weight at the jaw (F_{jaw}) for the EDGE experiment. Figure 2.5(b) shows the plot for 500g extracted in 2D.

2.1.3 Interpretation and Conclusion

For the MSEG, the strong ($R = 0.9999$) linear correlation obtained verified the accuracy of the strain gage on the proximal end. A good correlation for the distal end ($R = 0.9843$) suggested a linear fit may be acceptable for the specific, fixed handle position. Equation 2.1 and Equation 2.2 show the relationship between the measured strain and the applied force at grasper handle and grasper jaw respectively. In both equations,

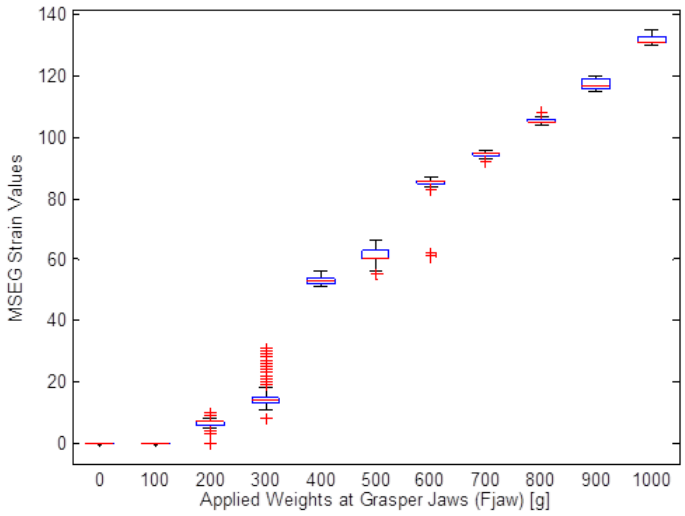

Figure 2.4: Box plot of applied weights at grasper jaws (distal end) vs measured strain values for the MSEG

$Strain_{d,fixed}$ and $Strainp, fixed$ denote the strains at proximal and distal ends, while F_{handle} and F_{jaw} denotes the applied forces at proximal and distal ends.

$$Strain_{p,fixed} = 0.44382F_{handle} \tag{2.1}$$

$$Strain_{d,fixed} = 0.14655F_{jaw} - 12.545 \tag{2.2}$$

However, we observed inconsistencies on the values reported by the strain gauges for separate experiments. This finding implies that the strain gage force-measuring mechanism of the MSEG is unreliable and requires a better design for measuring force.

The F_{meas} and F_{jaw} at the EDGE grasper in Figure 2.5(a) demonstrate a non-linear relationship that is highly dependent on the jaw angle. Figure 2.5(b) indicates considerable hysteresis within each cycle of grasper jaw angles: for the same jaw angle measured force differs between"grasping" and "releasing". While a multidimensional surface regression can be used to approximate the mapping (Equation 2.3). The hysteresis suggests this would be inaccurate unless it accounts for direction of grasp (Equation

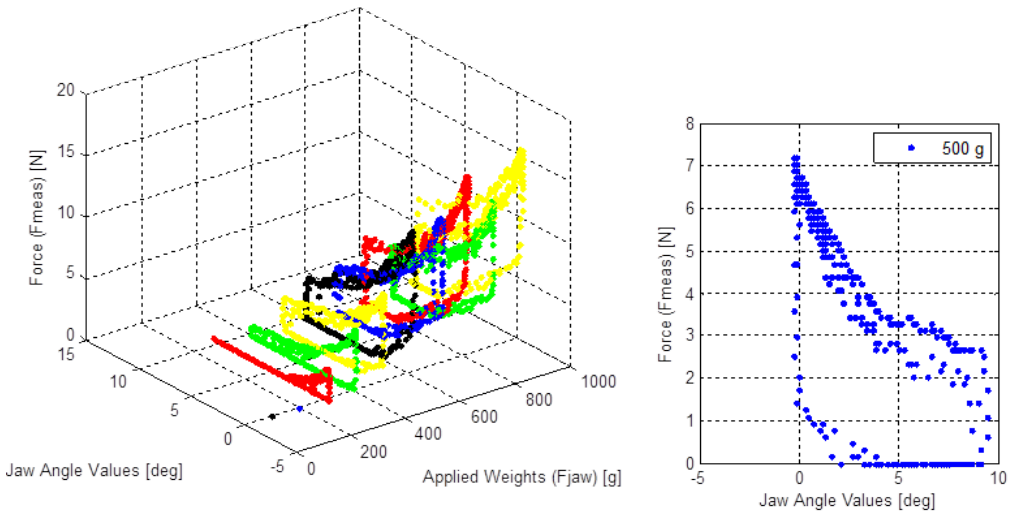

(a) At different applied weight intervals

(b) At 500g applied weight

Figure 2.5: Measured force values vs jaw angle at different applied weight intervals over full swipe handle position for the EDGE grasper

2.4). θ_{jaw} is the measured angular displacement (opening angle) of the between the two jaws of the grasper, and t is time.

$$F_{jaw} = f(F_{meas}, \theta_{jaw}) \tag{2.3}$$

$$F_{jaw} = f(F_{meas}, \theta_{jaw}, t) \tag{2.4}$$

During the data collection for MSEG experiments, we observed multiple inconsistencies in the raw strain gage readings recorded via the GUI for the same amount of applied weights under the same loading condition. This finding motivates us to develop a new hardware and software implementation with its own GUI for sending commands to motor and collecting data from the sensors of the MSEG. This new system was developed using *LabVIEW* and presented in Chapter 3.

We conclude that measurement of applied force at the tool-tissue interface via proximal sensors is confounded by grasper position, direction-dependent friction, and mechanism parameters. Unless these influences can be reliably accounted for, this work

motivates direct measurement of forces at the distal end (jaws) directly at the tool-tissue boundary. This would require novel sensors to be developed. Further studies employing proximal sensors should take into account differences in angle of force acting on the grasper within each grasping motion.

2.2 Alternative Methods for Direct Force Quantification at Grasper Jaws

Experiment in the previous section suggested that indirect calculation of distal force at grasper jaws from proximal force measurement at grasper handle is error-prone and requires consideration of various factors. This fact motivates measurement of force directly at grasper jaws, or direct measurement of force that is actually delivered to the tissue. In this section, we present an alternative low-cost method for quantifying forces at the tissue directly. The following section would be largely based on the paper presented in [49].

2.2.1 Pressure Indication Microcapsules Sheet

We propose a low-cost method for reality-based training (i.e., the use of real tools in physical tissue phantoms or porcine training models) where an accurate, quantifiable indicator of tissue damage can be inexpensively deployed at any physical tool-tissue interface. Our method utilizes dye-impregnated microcapsules that burst at a tunable pressure resulting from an applied force to provide a continuous measure of pressure-related damage. We herein compare two microcapsule deployment techniques: indicator sheets and indicator slurries to determine their relative feasibility as markers for tool-tissue pressure indication for use in surgical training and skill assessment.

Experimental Protocol

A polyester-based Prescale pressure sensing film (4LW, Fujifilm Holdings Corp, Tokyo, Japan) microcapsule indicator was used. Custom color intensity calibration of Prescale was performed. The double-layered pressure sensing films were placed on top of a flat glass base. A 0.25inx0.952in gage block (614212, Mitutoyo America Corp, Aurora, IL)

was stacked on top of the pressure sensing films (test site) and standardized fixed weights were subsequently applied. The weights were applied to five different test sites, linearly separated by 1.5cm. The applied weights ranged from 200g to 1000g at increments of 200g for each test site. We repeated the same experiment, adding a single-layered synthetic bowel tissue made from silicon rubber (LGI-10, Simulab Corporation, Seattle, WA) between the glass piece and the pressure sensing films. The experiment test bed of the calibration process and pressure indication experiment with bowel tissue is shown in Figure 2.6(a).

The Mechanical Smart Endoscopic Grasper (MSEG) developed by Roan et al. [6] was used with identical settings and calibration established in [11, 6]. The device was used to apply and measure constant single-grasps to synthetic bowel tissue with no overshoot. The test bed consisted of suspending the bowel tissue from two pedestals 3cm apart, placing the Prescale on top of the tissue, and applying a constant, measured force level for about 2 minutes to each test site (linearly separated by 2cm). The target force levels ranged from 1.5 Newton (N) to 3.5N at increments of 0.25N. An image of the test bed before any grasps were executed appears in Figure 2.6(b).

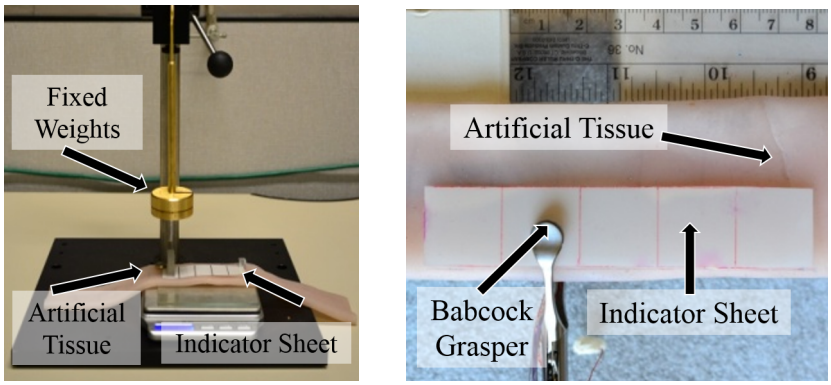

(a) Fixed weight experiment (b) MSEG experiment

Figure 2.6: Setup for pressure indication experiments on phantom bowel tissue

After at least 20 minutes had elapsed, photos of the indicator sheets were taken with a digital camera (D3100, Nikon Corp, Tokyo, Japan) under standard office lighting conditions. The resulting files were processed with ImageJ and MATLAB into a 258x882pixels (7.5x25.64mm) 8-bit image individually to quantify the color intensity

in different regions via the colormap tool. The intensity was linearly normalized to be between 0 and 1.

Results

Figure 2.7 shows the digitally extracted colormap distribution of the pressure gradient from the Prescale pressure sensing films. Table 2.1 shows the resulting quantities. The mean intensity was calculated over all pixel values in each test site image, and the affected area was computed by summing all pixel areas that exhibited values above the baseline threshold of no applied pressure.

Table 2.1: Normalized Mean Intensity and Calculated Area of Colored Pixels for Calibration and Pressure Indication Experiment with Fixed Weight and MSEG

Fixed	Calibration		Pressure Indication Experiment	
Weights (g)	Mean Intensity	Area (mm^2)	Mean Intensity	Area (mm^2)
200	0.0076664	58.9248	0.0015745	15.5763
400	0.0115272	81.2633	0.0030090	23.0213
600	0.0183892	101.1590	0.0036755	32.4979
800	0.0206257	120.4460	0.0118303	119.6830
1000	0.0335509	143.2900	0.0139008	125.3660
Pearson's R	0.9661	0.9996	0.9387	0.9175
	($p < 0.01$)	($p < 0.00001$)	($p < 0.02$)	($p < 0.03$)
Spearman's ρ	1	1	1	1
	($p < 0.02$)	($p < 0.02$)	($p < 0.02$)	($p < 0.02$)

MSEG	Pressure Indication Experiment	
	Mean Intensity	Area (mm^2)
Pearson's R	0.71 ($p < 0.03$)	0.87 ($p < 0.003$)
Spearman's ρ	0.78 ($p < 0.01$)	0.88 ($p < 0.003$)

Interpretation and Discussion

We expected to see a monotonic increase in overall intensity for each test in the indicator sheet (Figure 2.7). While there is an overall trend of increase (Spearmans $\rho =$ 1 and 0.78 in Table 2.1), there are several deviations from a purely monotonically increasing trend. The patterns in Figure 2.7 show the pressure distribution in much finer

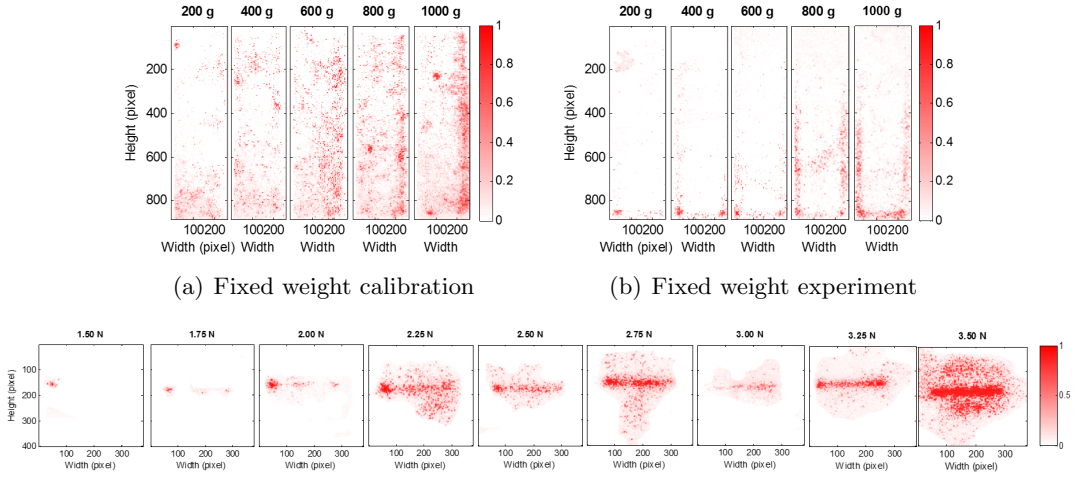

(a) Fixed weight calibration

(b) Fixed weight experiment

(c) MSEG experiment

Figure 2.7: Pressure gradient colormap for pressure indicator sheet experiments

spatial resolution (0.1mm according to the manufacturer) than the single grasper force measurement provided by the MSEG, revealing that only the first row of grasper jaw "teeth" engage the tissue a high force due to the angle of incidence. This illustrates that even if the MSEG force sensor was accurately calibrated, the computation of applied pressure distribution may be inaccurate if done with simple assumptions about grasper area, angle of engagement, and tool-tissue orientation. We suspected the force levels indicated by the MSEG were less accurate than those derived from the indicator sheet approach. Our claim was verified by the data obtained from the pressure indication experiment with fixed weights, showing Spearmans $\rho = 1$, a higher correlation than for the MSEG $\rho = 0.78$.

Limitations of the microcapsule approach include time and repeatability requiring a readily replaceable and disposable solution. We conclude that the microcapsule approach may provide an inexpensive, quantitative method of measuring surgical tool-tissue pressure distribution at a high spatial resolution and that this approach merits further study.

2.3 Conclusion

This chapter indicates that using proximal sensors to measure distal forces exerted by a grasper on tissue is error-prone. If no distal force sensors are available, a thorough kinematic analysis is required to account for all sources of error. Most notably the mappings of grasper force F_{jaw} and displacement d_{jaw} must both depend on distal inputs (handle force F_{handle} and angle θ_{handle}). Moreover, the MSEG software was proved to be unreliable and a new hardware and software solution for robust data collection is required.

Chapter 3

Hardware and Software Development

This chapter provides a detailed explanation on hardware and software implemented in this work, as well as the interface between software to hardware and hardware to user.

3.1 The Mechanical Smart Endoscopic Grasper

In this work, an instrumented laparosopic grasper developed by Roan et al [6], the mechanical smart endoscopic grasper (MSEG) is used and implemented. The MSEG is developed based on its predecessor: the motorized endoscopic grasper (MEG) [2, 4].

3.1.1 MSEG Kinematic Mechanism

The MSEG consisted of a laparoscopic tool with scissor linkage mechanism and a Babcock grasper head (#33510 BL, Karl Storz GmBH & Co. KG, Tuttlingen Germany). The mechanism is actuated through a pushrod that is connected to a partial pulley via ball bearing. The partial pulley is wrapped with a 0.024 inch uncoated stainless steel cable (#2024, Sava Industries Inc, Riverdale NJ) to a capstan, that is driven by a brushed DC motor (RE25, Maxon Motor AG, Sachseln, Switzerland) through a 19:1 planetary gearbox (GP26, Maxon Motor AG, Sachseln, Switzerland). Figure 3.1 shows the configuration of the MSEG.

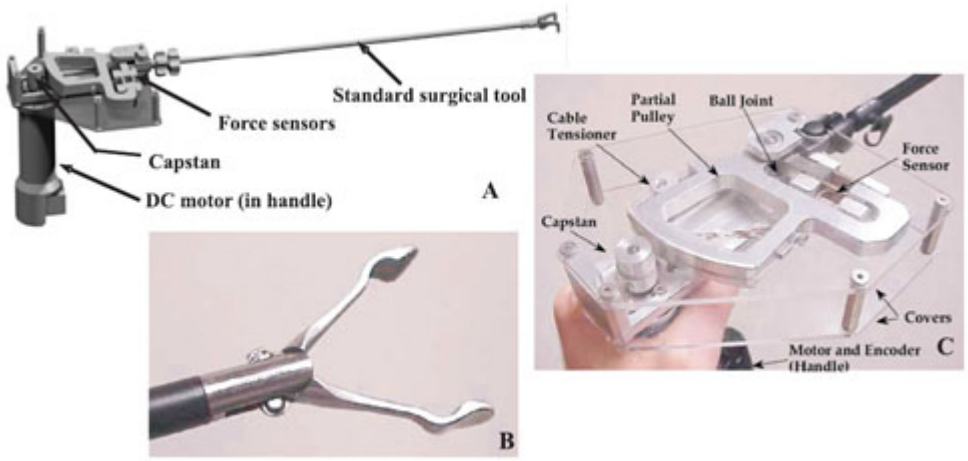

Figure 3.1: (a) CAD Drawing of the MSEG (b) close up view of the Babcock grasper (c) Driving mechanism of the MSEG [5]

3.1.2 MSEG Sensors and Actuators

The MSEG consisted of several sensors that are capable of measuring various tissue properties that indicates ischemic or healthy tissues. From the MEG, there is a pair of parallel strain gages (FBB300, 40lb, FUTEK Advanced Sensor Technology, Inc, Irvine, CA, USA) that measure the force at the partial pulley (proximal end), and a 500 count-per-revolution (CPR) rotary differential encoder (HEDL-5540#A02, Avago Technologies, San Jose, CA, USA) that is connected to the same shaft as the motor measures the angular displacement of the grasper jaws. The MSEG features additional sensors that are packed into a 7mm by 7mm sensor head as shown in Figure 3.2. It consisted of a thermistor that measures temperature, a photodiode and four LEDs to measure tissue optical impedance, and four gold plated electrodes that measure electrical impedance. In this work, only the strain gages and the encoder (force and displacement sensors) are used since our scope is limited to mechanical properties of tissue.

The MSEG is driven with a DC motor that is connected to a linear four-quadrant DC servo-amplifier (LSC 302, Maxon Motor AG, Sachseln, Switzerland). The strain gages are connected to a strain gage amplifier (JM-2, FUTEK Advanced Sensor Technology, Inc, Irvine, CA, USA). The strain gages are aligned in a double beam configuration to

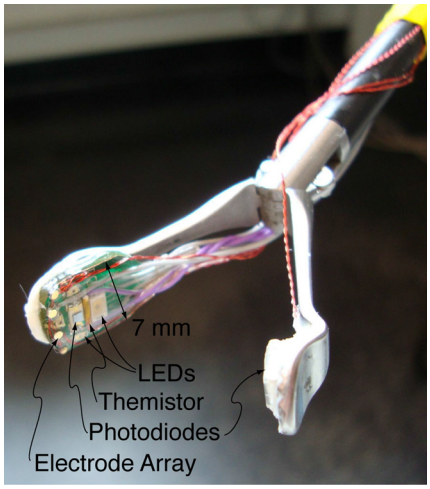

Figure 3.2: Close up view of the MSEG sensor head [6]

eliminate sensing of torque due to bending moment.

3.1.3 MSEG Software and Graphical User Interface

In [6], Roan et al. developed a graphical user interface (GUI) that allows user to send force commands to the motor and read corresponding sensor values. The software or code for controlling the MSEG was written in *Linux C++* and the GUI is created using *QT Creator*. Figure 3.3 shows a snapshot of the GUI.

3.2 The *Smart Tool* - Modifications of the Mechanical Smart Endoscopic Grasper

In this work, the MSEG developed by Roan et al in [6] is modified. Most of the existing sensors from the MSEG are preserved, especially the force and displacement sensors. The sensors packed in the sensor head are removed. Additional touch sensors are added to the MSEG to enable detection of initial contact between grasper jaws and tissue. Also, the sofware and GUI for the modified MSEG are completely rewritten. This is done after extensive experimental testing and low-level code review indicated that the

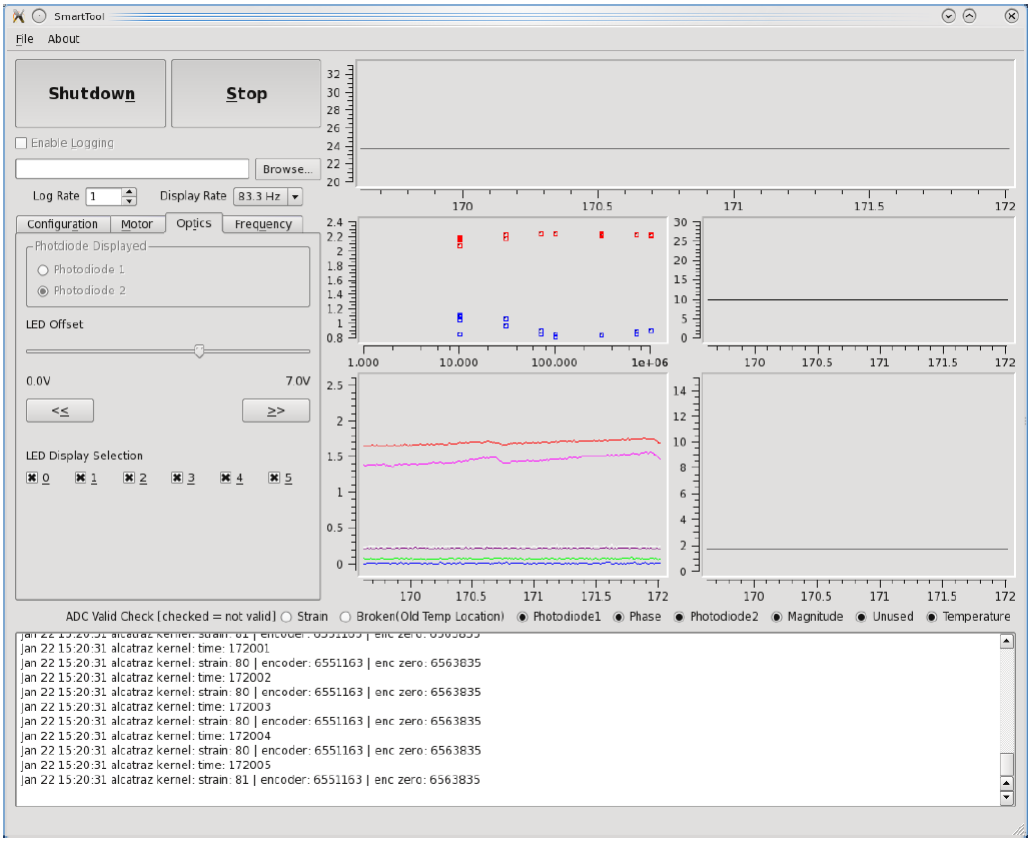

Figure 3.3: Screen capture of Roan's original MSEG GUI with (clockwise from top) temperature chart, jaw displacement chart, grasp force chart, optical absorption chart, and impedance chart [6]

MSEG platform was unstable and introduced artifacts in data collection. This modified MSEG is subsequently referred to as the *Smart Tool* throughout this work.

3.2.1 MSEG Hardware Modifications

The kinematic mechanism of the original MSEG is preserved in this work. The actuating motor-drive remains unchanged. As for the sensors, only the strain gage and encoder remain, while the other sensors packed in the sensor head (thermistor, photodiode, LEDs, and gold plated electrodes) are removed as they are irrelevant to the purpose of

this work.

In addition to the existing sensors, two touch sensors (1129_1, Phidgets Inc, Calgary, Alberta, Canada) are added to the MSEG. Each of the touch sensor is connected with a piece of insulated wire that is wrapped in between the "teeth" of the grasper jaws. Figure 3.4 shows the touch sensor configuration on the MSEG. The purpose of the touch sensor is to detect the moment when the grasper jaws are in contact with an object or a tissue. This will help detecting the initial tissue thickness and actual tissue displacement as opposed to total jaw displacement.

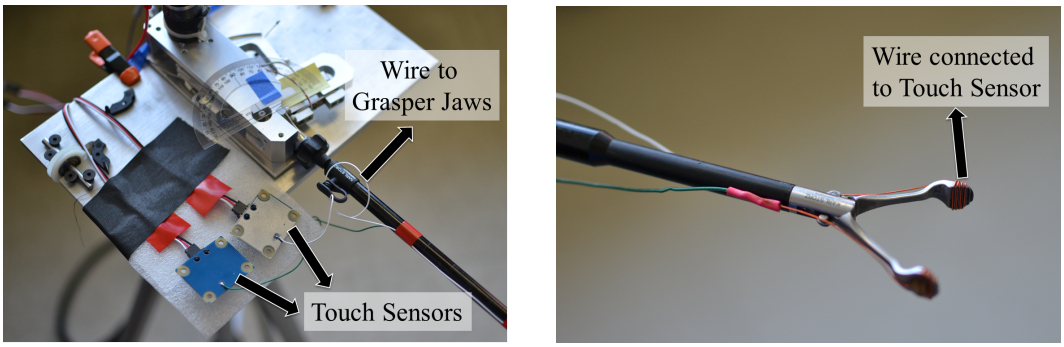

(a) Touch sensors board

(b) Wire wrapped around grasper jaw teeth connected to touch sensor

Figure 3.4: Touch sensors configuration

3.2.2 MSEG Software and Hardware-Software Interface Modifications

The MSEG software is completely modified from the original software developed by Roan et al in [6]. Due to inconsistencies in the recorded sensor readings in the original GUI (explained in Chapter 2), a new GUI and hardware-software interface, and data collection is developed in *LabVIEW*.

The hardware is interfaced to a *Windows* operating system (OS) computer using the PCI6230 module from *National Instruments*. The module has eight analog input, four analog output, two counter, six digital input, and four digital output channels. Two channels of the PCI6230 analog outputs are connected to Pin 7 and 8 of the DC servo-amplifier. The two outputs from strain gage is connected to two analog input channels of PCI6230. Both the motor and the strain gages are powered with 5V voltage

via the circuit board developed by Brown et al. and Rosen et al. in [2, 4]. Meanwhile, only channels A and B of the encoder are used and connected to two digital inputs of PCI6230. Each of the touch sensors is connected directly to one analog input channel of PCI6230. The encoder and touch sensors are powered using a Phidget USB board (1047_0, Phidgets Inc, Calgary, Alberta, Canada), connected to a USB port of the computer, to supply a constant 5V power (the current required by the encoder 85mA exceeds the output of the PCI6230 10mA). The ground pin of the Phidget USB board is connected to the digital ground of PCI6230 to ensure a common electrical ground for both devices.

All the analog input channels of PCI6230 are set to operate in "differential" mode, and all analog output channels are set to operate in "reference single-ended (RSE)" mode in *LabVIEW*. Figure 3.5 shows the pin connection diagram for PCI6230, and Figures 3.6 and 3.7 show the photo of the actual wiring connection from PCI6230 to MSEG hardware.

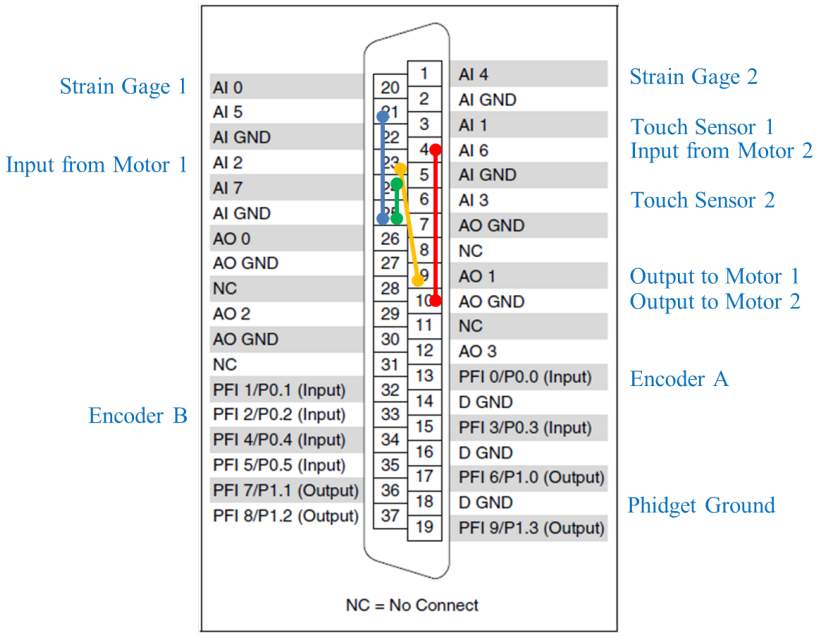

Figure 3.5: Pinout of PCI6230

Figure 3.8 and Figure A.1 show the front panel and the block diagram of the custom

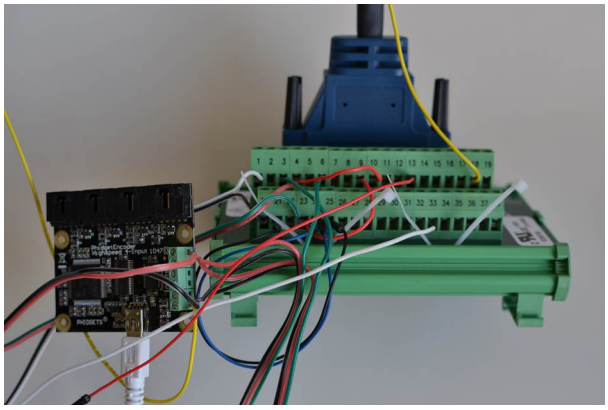

Figure 3.6: Photo of connection to PCI6230 board

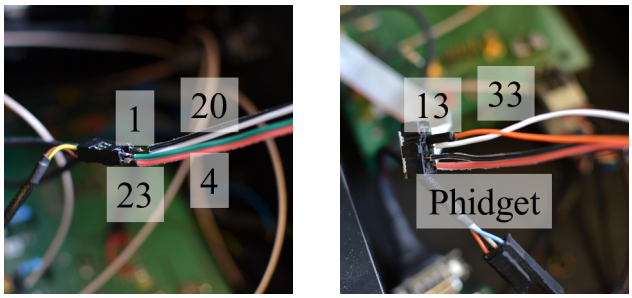

(a) Strain gage and motor (b) Encoder

Figure 3.7: Cable connection from PCI6230 board with numbers adjacent to cables indicating respective PCI6230 pin number connected

LabVIEW GUI respectively. Output signal to the motor can be set as various types of waveforms (sinusoidal, square, triangle, or trapezoidal) with maximum and minimum of 5V and -5V. The *LabVIEW* voltage command is being sent to the motor amplifier which converts the voltage into the corresponding current that powers the motor. In Figures 3.8 and A.1, the output signal is set to be a trapezoidal waveform with amplitude and frequency that can be determined by user. The output waveform sent to motor is displayed on a graph as shown in Figure 3.8. In the front panel, sensors data are shown in the lower graph. Also, in the same graph, the actual signal that is being written to the motor is measured and displayed. The strain gage and touch sensors readings are

displayed as voltage values with the range from -5V to 5V, while the encoder reading is displayed in degrees.

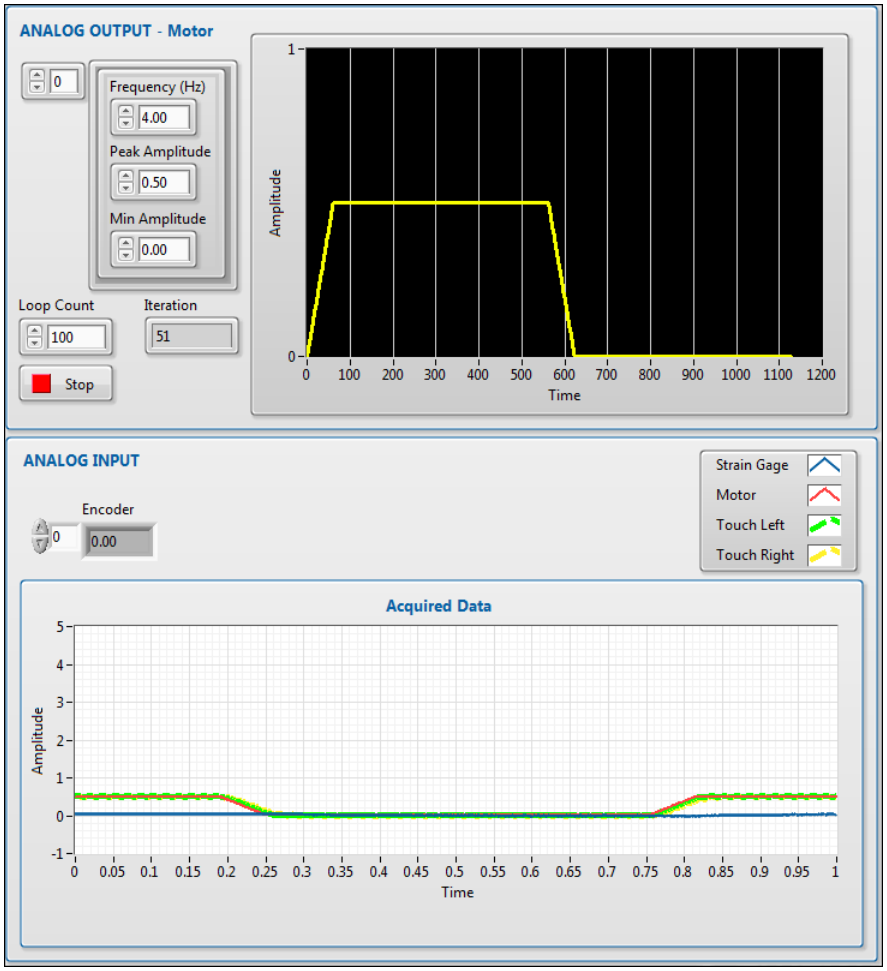

Figure 3.8: Front panel of *Smart Tool* GUI in *LabVIEW*

All the output signals are sent at a sampling rate of 1kHz, and all the input signals are read at the same sampling rate of 1kHz. Also, the GUI is capable of recording all the output data at the analog outputs and input data from the analog and digital inputs into a file with precise timestamp every 1ms. In this work, data are saved as *.lvm* (*LabVIEW* Measurement extension) file type to allow easier data processing in *MATLAB*.

3.3 MSEG Calibration

In order to understand and process the data from the motor and sensors, calibrations have to be performed to convert all raw voltage data into data with the correct units. Also, additional conversions from readings detected at the sensor (grasper handle) to actual values translated to the tissue (grasper jaws) are required.

3.3.1 Motor Command to Motor Force Relationship

In the *Smart Tool*, force at the handle is the result of an actuation from the motor. Thus, in order to gage the actual amount of force that is applied to the handle, we perform a calibration that maps motor input command to the resulting force produced at the handle. Using the developed *LabVIEW* GUI, we apply discrete motor command values to the motor incremented by 0.1V from 0V to 3V. Each commanded voltage is mapped to a current by the motor amplifier. At each command value into the motor, the resulting voltage reading from the strain gage is recorded. At all points in the experiment, the grasper jaws are fully closed and empty. The resulting motor command and strain gage voltage values are plotted as box plot distribution, shown in Figure 3.9. Note that there is a zero offset value for the strain gage voltage in no load condition, and all points in the plot shown in Figure 3.9 has been subtracted with the zero offset value.

Curve fitting is performed in *MATLAB* by fitting a second order exponential equation that relates the strain gage voltage to motor voltage. The curve fitting equation is shown in Equation 3.1, where $V_{straingage}$ is the strain gage output voltage, and $V_{command}$ is the motor input voltage (thus commanded current). This curve fit equation results in a root mean squared error (RMSE) of 0.04421 (Spearman's $\rho = 0.9974$, $p < 4.055 \times 10^{-6}$). Figure 3.10 shows the plot of motor voltage versus strain gage voltage median values, overlaid with the fitted curve.

$$V_{straingage} = 2.022e^{-0.01523V_{command}} - 2.052e^{-1.105V_{command}} \tag{3.1}$$

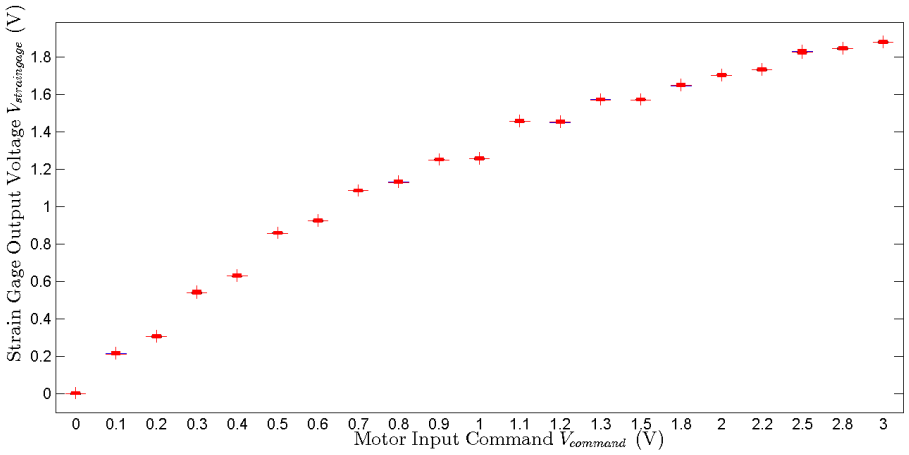

Figure 3.9: Box plot of input command to motor versus output voltage from strain gage

3.3.2 Force Calibration

Raw strain gage data are recorded as voltage values in *LabVIEW*. In order to map the voltage values to meaningful force values, we performed a force calibration experiment. The experimental protocol for force calibration is to that of MSEG proximal force quantification experiment described in Section 2.1.1 of Chapter 2. The only difference is the GUI and the *National Instruments* hardware used for data collection. The *LabVIEW* GUI developed in this work is used to collect voltage data from strain gage. The applied incremented weights are plotted versus the measured strain gage values, as shown in Figure 3.11. The fit is acceptable with root mean square error (RMSE) of 0.2691 (Pearson's R = 0.9914, $p < 0.0001$). It is noted that the strain gage voltage at zero loading is non-zero. For data analysis, the strain gage voltage values are to be offset with the first reading when no loading is applied to the strain gage at the start of every new grasping or data recording session. The relationship between the voltage and the force are obtained by linear curve fitting in *MATLAB*, and the resulting fit after subtracting the offset is shown in Equation 3.2, where F_{handle} is the force at the handle in Newtons, and $V_{straingage}$ is the strain gage voltage in Volts.

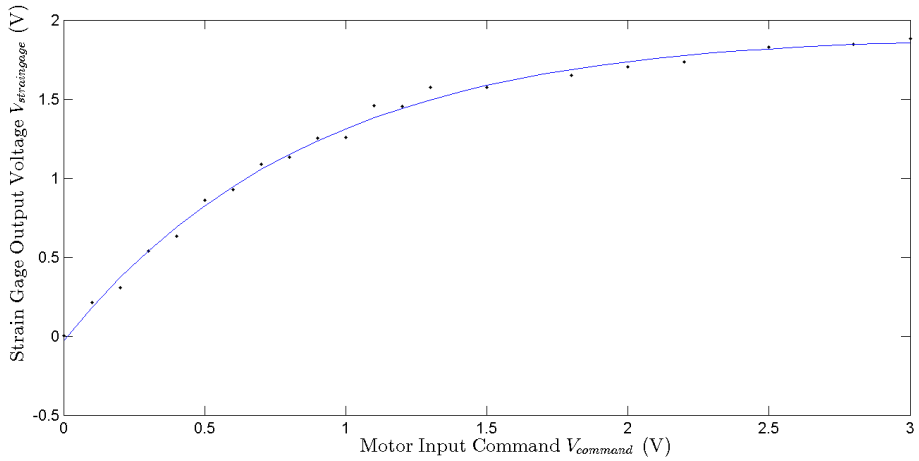

Figure 3.10: Plot of input command to motor versus output voltage median from strain gage together with the fitted curve

$$F_{handle} = 11.89 V_{straingage} \tag{3.2}$$

After the force at the handle is obtained, force at the grasper jaws that is delivered to the tissue are calculated using a nonlinear transfer function. The transfer function is derived based on static analysis of the grasper linkage mechanism. We assume that the force measured by the strain gage at the handle F_{handle} is equal to the force at pushrod F_p (Equation 3.3. Figure 3.12 shows a simplified handle - pushrod configuration, where r_{pp} is the radius of the partial pulley and a is the fixed perpendicular distance between the pushrod and the pivot.

$$F_{handle} = F_p \tag{3.3}$$

Next, we have to find the relationship between the force at the pushrod F_p and the force acting on the tissue at the grasper jaws F_{jaw}. Figure 3.13 shows the diagram of the grasper jaws connected to the pushrod via a scissor linkage mechanism. Figures 3.14(a) and 3.14(b) shows the free body diagram of the grasper jaw linkage and the pins

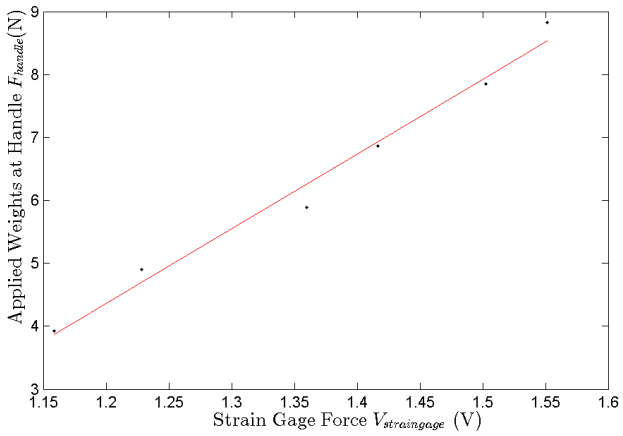

Figure 3.11: Plot of strain gage voltage versus applied weights at partial pulley (handle)

in the scissor linkages. Equation 3.4 shows the moment balance equation of the grasper jaw about the point in pin D location, relating $F_{jaw,normal}$ and F_{AC}. $F_{jaw,normal}$ is the force acting perpendicular of the grasper jaw. The force that is effectively delivered to the tissue is the vertical component of $F_{jaw,normal}$, denoted by F_{jaw}. Both vectors are related through trigonometric relationship shown in Equation 3.5. Equation 3.6 shows the force balance equation in pin A, relating F_{AC} and F_p.

$$\Sigma M_D = 0$$

$$(F_{AB}\cos\alpha)(L_2\sin\beta) + (F_{AB}\sin\alpha)(L_2\cos\beta) + F_{jaw,normal}L_{jaw} = 0$$

$$F_{jaw,normal} = \frac{L_2}{L_{jaw}}F_{AC}(\sin\alpha\cos\beta + \cos\alpha\sin\beta) \tag{3.4}$$

By trigonometric identity,

$$F_{jaw,normal} = \frac{L_2}{L_{jaw}}F_{AC}\sin(\alpha+\beta)$$

$$F_{jaw} = F_{jaw,normal}\cos\theta_{jaw} \tag{3.5}$$

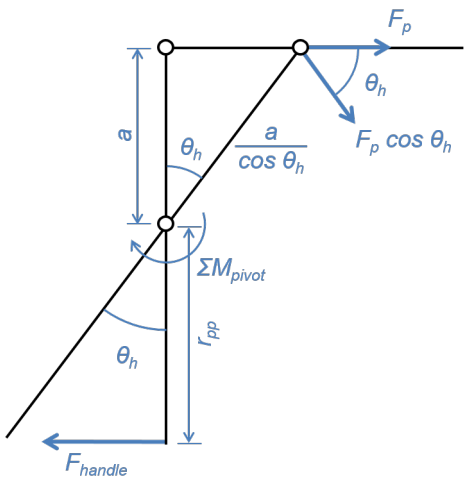

Figure 3.12: Free body diagram of the partial pulley (handle) and pushrod

$$\begin{aligned} \Sigma F_x &= 0 \\ F_{AC} \cos \alpha - \frac{F_p}{2} &= 0 \\ F_{AC} &= \frac{F_p}{2 \cos \alpha} \end{aligned} \tag{3.6}$$

It should be noted that α, β, and θ_{jaw} are the instantaneous angles at unique jaw positions. α and β can be related through the law of sines. The instantaneous angle β is simply the intial angle β_0 at which the grasper jaws are fully closed ($\theta_{jaw} = 0$), plus the instantaneous jaw angle θ_{jaw}. This is because the grasper jaw (link L_2 and link L_{jaw}) is a single rigid body with an offset angle of β_0 at the pivot. These two relationships are shown in Equation 3.7.

$$\begin{aligned} \alpha &= \sin^{-1}\left(\frac{L_2}{L_1} \sin \beta\right) \\ \beta &= \beta_0 + \theta_{jaw} \end{aligned} \tag{3.7}$$

Combining Equations 3.3, 3.4, 3.5, and 3.6, we obtain the transfer function that

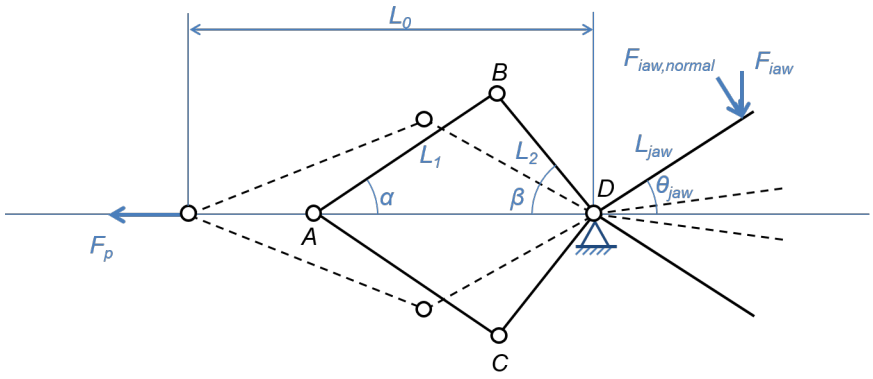

Figure 3.13: Free body digaram of grasper jaw connected to pushrod via scissor linkage mechanism

relates the force measured at the strain gage F_{handle} to the force delivered to the tissue at the grasper jaws F_{jaw} for a given grasper jaw angle θ_{jaw}. This is shown in Equation 3.8. The constants used in this equation appear in Table 3.1.

$$F_{jaw} = \frac{L_2}{2L_{jaw}} F_{handle} \left(\frac{R_{pp}}{a}\right) \left[\tan\left\{\sin^{-1}\left(\frac{L_2}{L_1}\sin\left(\beta_0 + \theta_{jaw}\right)\right)\right\} \cos\left\{\sin^{-1}\left(\frac{L_2}{L_1}\sin\beta\right)\right\} + \sin\left(\beta_0 + \theta_{jaw}\right)\right] \cos\theta_{jaw} \tag{3.8}$$

Table 3.1: The Measured Values of All Grasper Links Lengths and Other Relevant Grasper Geometry

Grasper Geometry Parameter	Values
r_{pp}	73.15 mm
a	10.1 mm
L_0	9.93 mm
L_1	4.9 mm
L_2	5.7 mm
L_{jaw}	27.88 mm
β_0	18.939°

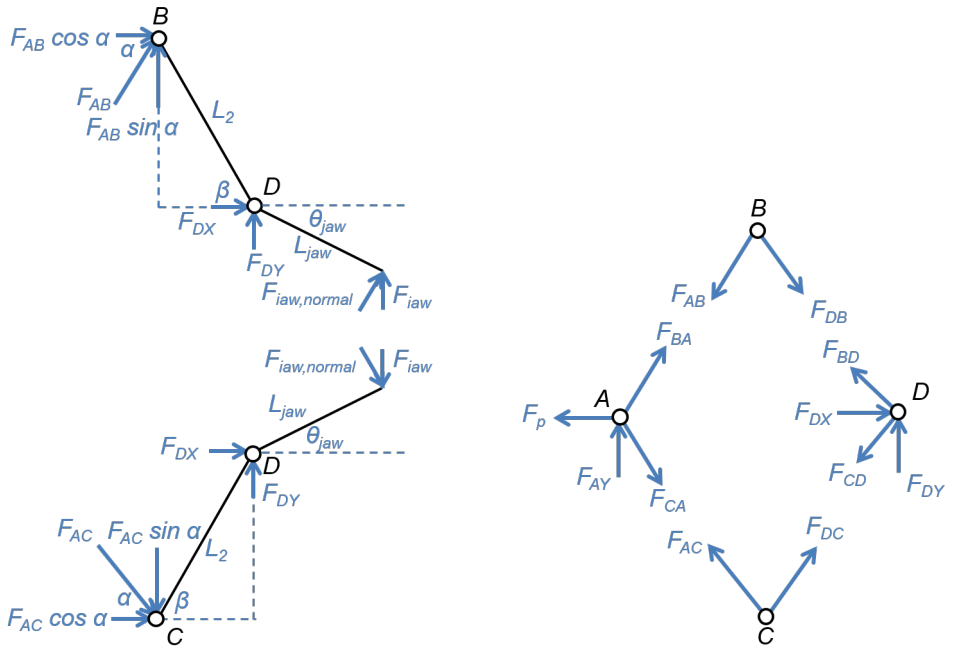

(a) A single grasper jaw (b) Each pins connecting the scissor linkage

Figure 3.14: Free body diagrams for grasper jaw and pins

Experimental Verification of Force Calibration

To verify the resulting force at grasper jaws calculated using the force transfer function in Equation 3.8, we perform an experiment to quantify the force directly at the grasper jaws. Using the GUI in *LabVIEW*, fixed amount of command voltage is given to the motor ranging from 0V to 2V at an interval of 0.1V. A digital scale with an accuracy of 0.001 g is placed in between the grasper jaws as shown in Figure 3.15.

At every command sent to the motor, the strain gage voltage values are stored in the log file and the resulting reading at the digital scale is noted after it stabilizes. Figure 3.16(a) shows the plot of scale reading in gram versus strain gage voltage in V, while Figure 3.16(b) shows the plot of scale reading in N versus strain gage voltage in N. From the two figures, it can be seen that the force at the grasper jaws are nonlinearly related to the force at the handle (strain gage), with the force sensed at the handle being almost about ten times larger than the force actually delivered to the tissue at the grasper jaws.

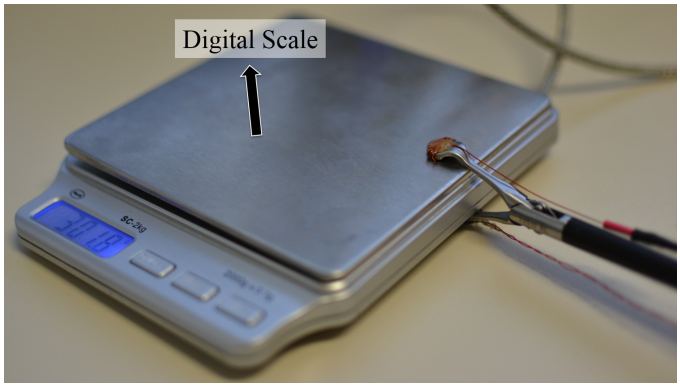

Figure 3.15: Setup of Force Calibration Verification

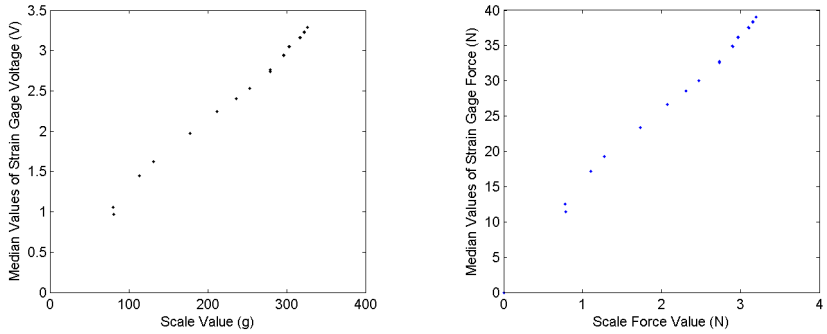

(a) V to g (b) N to N

Figure 3.16: Plot of Scale Reading versus Strain Gage Reading

3.3.3 Displacement Calibration

In *LabVIEW*, the encoder output is recorded in terms of degrees of revolution. These values are converted with the encoder counts per revolution (CPR) and the gearbox ratio of the motor such that the resulting degree values are equal to angle of revolution at the motor shaft, and stored in the log file. This requires a calibration that maps the angle of revolution from the motor shaft to jaw angle, and then jaw opening.

It is observed that the encoder reading is proportional to the force applied at the handle. The resulting jaw angle or jaw opening at the grasper jaws relate to the handle force as a nonlinear function. That is, as force increases, the encoder reading increases

even if the jaws are fully closed. To characterize the effect of handle force to the encoder reading, we perform an experiment whereby the grasper jaws are kept at three different constant jaw separation conditions: 1) fully closed, 2) grasping a gage block of thickness 6.34mm (614212, Mitutoyo America Corp, Aurora, IL), 3) grasping a cylinder incremental weight piece of thickness 11.55mm. Figure 3.17 shows the picture of the gage block and the weight piece.

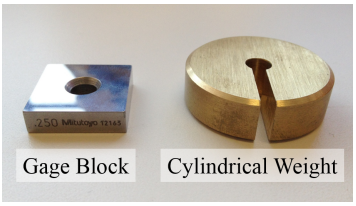

Figure 3.17: The gage block and cylindrical weight piece used for the force correction experiment

For each jaw separation, motor commands are applied from 0V to 2V at increments of 0.1V. Throughout the voltage application to the motor, the jaw separation is kept constant and unchanged. The process is repeated for three times for each jaw separation condition. Figure 3.18 shows the plot of strain gage voltage versus encoder angle for all three experiments at three different jaw separation conditions. By *MATLAB* curve fitting, it is obtained that Equation 3.9 represents the force correction angle $\theta_{correction}$ on the encoder angle reading.

The value of this force correction angle factor is subtracted from the raw encoder reading from *LabVIEW* (Equation 3.10). Next, the corrected angle value at the encoder θ_{enc} is converted to the angle value at the partial pulley / handle θ_{handle} as shown in Equation 3.11. The constant multiplier $\frac{18}{188}$ is obtained by measuring the maximum angular displacement of the partial pulley from the jaws fully opened to fully closed using a protractor, which is equal to 18°, and reading the corresponding encoder values from *LabVIEW*, which is equal to 188°.

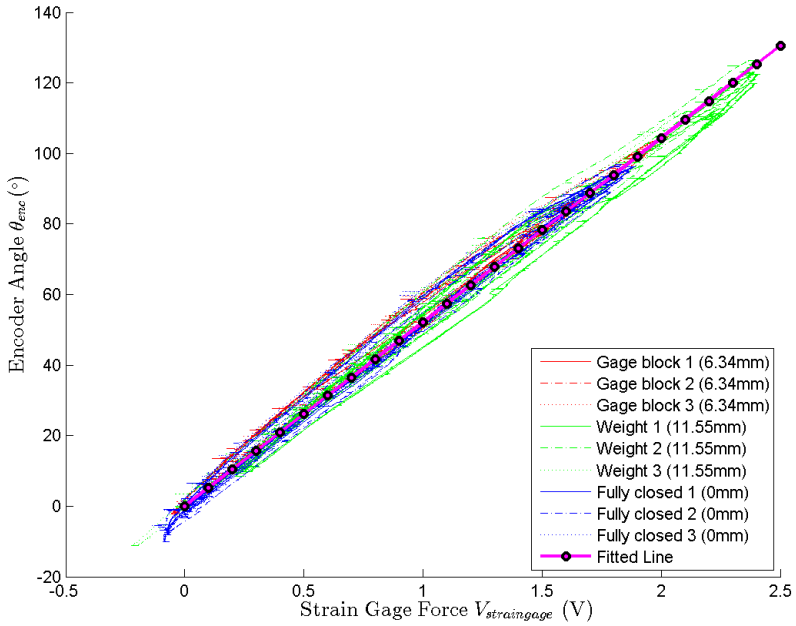

Figure 3.18: Plot of strain gage voltage versus encoder angle for all three jaw separation distances together with the fitted line used to derive the force correction factor for angle measurements

$$\theta_{correction} = 52.189 V_{straingage} \tag{3.9}$$

$$\theta_{enc} = \theta_{enc,raw} - \theta_{correction} \tag{3.10}$$

$$\theta_{handle} = \frac{18}{188}\theta_{enc} \tag{3.11}$$

Next, the transfer function that relates angular displacement at the handle and at the grasper jaws is derived using geometrical relationship of the grasper. By looking at the geometry of linkages at the partial pulley (handle) and pushrod (Figure 3.12), we obtain the relationship between handle angle θ_{handle} and linear displacement of pushrod x (Equation 3.12). Also, trigonometric analysis at the grasper jaws (Figure 3.19) obtains the relationship between the jaw opening or jaw linear displacement d_{jaw} and jaw angle θ_{jaw}, shown in Equation 3.13. Finally, in order to obtain the relationship between the

jaw angle θ_{jaw} and the pushrod displacement x, we use the law of cosines on the scissor linkage mechanism that connects the pushrod and the grasper jaws seen in Figure 3.19. This gives the following relationship as shown in Equation 3.14.

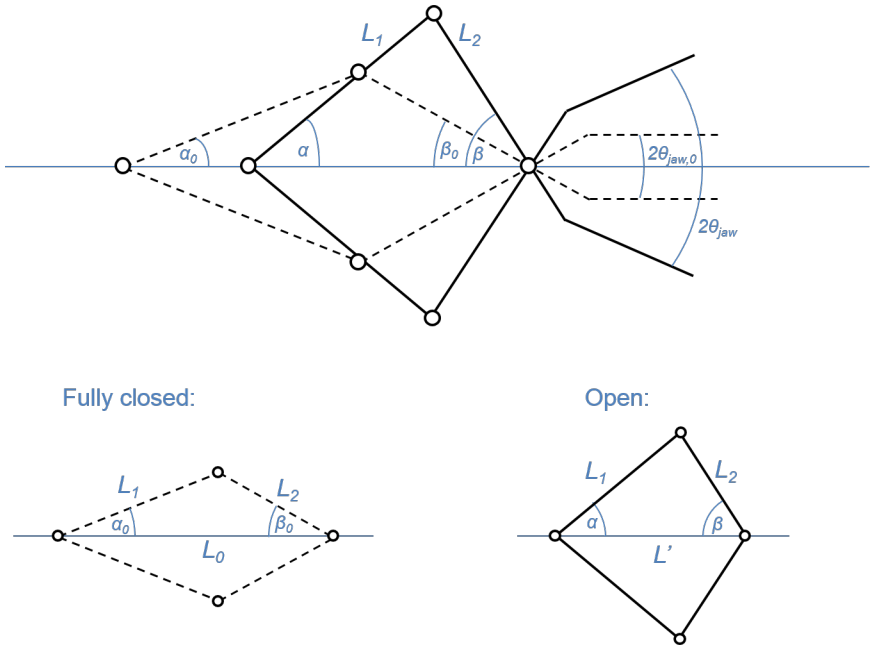

Figure 3.19: Linkage geometry of grasper jaws and scissor linkage mechanism drawn while fully closed and open

$$x = a\tan\left(\theta_{handle}\right) \tag{3.12}$$

$$d_{jaw} = 2L_{jaw}\sin\left(\theta_{jaw}\right) \tag{3.13}$$

$$\theta_{jaw} = -\beta_0 + \cos^{-1}\left(\frac{2L_2L_0\cos\beta_0 + x^2 - 2L_0x}{2L_2\left(L_0 - x\right)}\right) \tag{3.14}$$

Substituting Equations 3.12 and 3.14 into Equation 3.13, we obtain the closed form transfer function from handle angle θ_{handle} to jaw opening or jaw displacement d_{jaw},

depicted in Equation 3.15.

$$d = L_{jaw} \sin \left[-\beta_0 + \cos^{-1} \left(\frac{2L_2 L_0 \cos \beta_0 + \left(a \tan \left(\theta_{handle}\right)\right)^2 - 2L_0 a \tan \left(\theta_{handle}\right)}{2L_2 \left(L_0 - a \tan \left(\theta_{handle}\right)\right)} \right) \right] \tag{3.15}$$

Using Equation 3.15, it is obtained that the maximum jaw angle of $\theta_{jaw,max} = 54.075^\circ$ leads to a maximum jaw opening of 25.347mm. Both values are confirmed by measurement.

3.3.4 Filtering of Raw Data

Prior to implementation and calibration, raw data from strain gage and encoder is filtered with a second order Butterworth filter with cutoff frequency of 10Hz. The cutoff frequency is selected such the noise in the measurement data is filtered. The value is selected based on the work performed in [50], in which 10Hz and above are the range of frequency of surgical signals.

3.3.5 Summary of Calibration

The calibration process from filtered raw strain gage and raw encoder data to meaningful force delivered to the tissue at grasper jaws F_{jaw} and jaw displacement d_{jaw} can be summarized as a flowchart in Figure 3.20. Accurate computation of these values is crucial for correctly deriving stress and strain relationships.

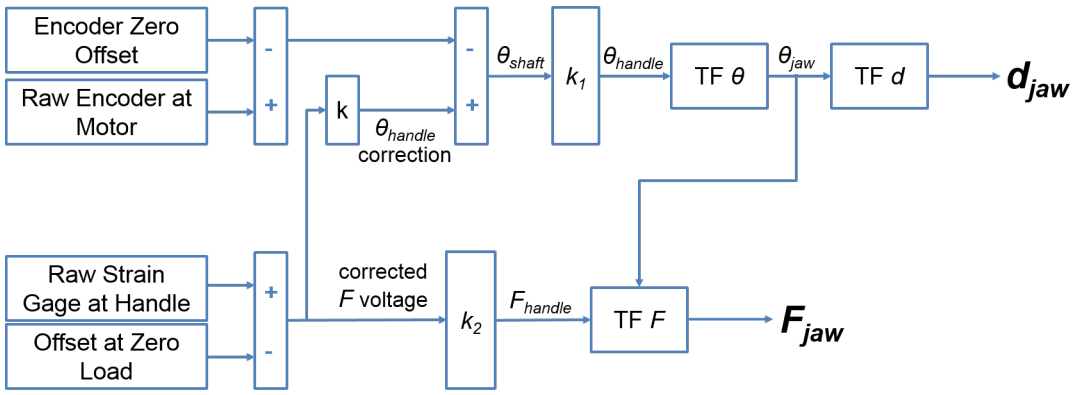

Figure 3.20: Flowchart of calibration process from raw strain gage and encoder data to force and displacement at tissue

Chapter 4

Development of an Extended Kalman Filter for Online Tissue Identification

Online tissue identification during surgical grasping is important. In order to prevent tissue injury due to excessive grasping, the exact tissue type has to be identified to determine the maximum force threshold of the tissue. Furthermore, this has to occur online and sufficiently fast in the early part of a grasp to mitigate damage before tissue-specific force thresholds are reached. Thus in this chapter, we present an extended Kalman filter (EKF) algorithm to estimate tissue parameters during grasping based on a tissue-specific model, and in turn identify tissue type being grasped based on the identified tissue parameters.

The two most commonly used methods for estimation processes are the recursive least squares (RLS) and Kalman filter. The RLS method is used for estimating *parameters* of static data that is slowly varing over time. Meanwhile, Kalman filters are used for estimating *states* of a dynamic data that varies over time. For the application of this work, the Kalman filter is chosen instead of the RLS estimator because the states of the system are changing over time (force and displacement of the tissue are able to vary significantly over time). Since Kalman filter is a state estimator, the tissue parameters to be estimated are augmented with the states.

At the end of this chapter, estimation of tissue parameters in simulation is attempted using the RLS estimator. The advantages and disadvantages of RLS as compared to EKF methods are then compared.

4.1 The Extended Kalman Filter

The Kalman Filter [51] is a method to estimate the states of a process for a linear discrete-time system by minimizing the mean of the squared error. For nonlinear systems, the extended Kalman fiilter (EKF) is used to perform such states estimation. The Kalman filter consists of the two stages: **time update** (prediction) in which the states and error covariance of the next time step is "predicted", and **measurement update** (correction) in which the estimated states from time update is "corrected" using measurement values and the Kalman gain. The process is repeated in a cycle until for all measurement data in real time, until better estimates of states are obtained. For nonlinear system, the Kalman filter algorithm is extended into the extended Kalman filter (EKF). In EKF, the nonlinear system is linearized at every iteration (time update) about the current states (states obtained from the measurement update of the previous time step), and the error covariance is updated subsequently following the linearization.

4.1.1 Time / System Model

A mathematical dynamic model of tissue during grasping is approximated in [43] as shown in Equation 4.1, where u is the applied force to the tissue (N), x is tissue displacement (m), m is mass of tissue grasped (kg), d is tissue damping coefficient (kg s^{-1}), and α and β are tissue stiffness coefficients (N and m^{-1}). This model employs Equation 1.1 over Equation 1.2 because the marginal increase in accuracy (increase of R^2 is 0.05%) is not justified given the added identification burden to the EKF.

$$u = m\ddot{x} + d\dot{x} + \alpha(e^{\beta x} - 1) \tag{4.1}$$

$$\ddot{x} = f(\mathbf{x}) + g(\mathbf{u}) = -\frac{d}{m}\dot{x} - \frac{\alpha}{m}(e^{\beta x} - 1) + \frac{1}{m}u \tag{4.2}$$

The system mode can be re-written as Equation 4.2 and restated as a state-space model in the continuous-time linear form as shown in Equation 4.3. $\mathbf{x} = \begin{bmatrix} x & \dot{x} & \alpha & \beta & d \end{bmatrix}^T$

is the state vector. α, β, and d are augmented to the state vector such that the three parameters are to be estimated with the EKF. $\mathbf{u} = \begin{bmatrix} u & 0 & 0 & 0 \end{bmatrix}^T$ is the input vector. $\mathbf{w} = \begin{bmatrix} 0 & w_\alpha & w_\beta & w_d \end{bmatrix}^T$ is the disturbance vector of process noise that enters α, β, and d. F and G are the continuous-time state and input matrices.

$$\dot{\mathbf{x}} = F\mathbf{x} + G(\mathbf{u} + \mathbf{w}) \tag{4.3}$$

The state matrix F is obtained by taking the Jacobian of the state equation (Equation 4.2), while the input matrix G is shown in Equation 4.5. The hat notation ($\hat{\mathbf{x}}$) denotes estimated variables.

$$F = \left.\frac{\partial f(\mathbf{x})}{\partial \mathbf{x}}\right|_{\mathbf{x}=\hat{\mathbf{x}}(t-1)} = \begin{bmatrix} 0 & 1 & 0 & 0 & 0 \\ -\frac{1}{m}\hat{\alpha}\hat{\beta}e^{\hat{\beta}\hat{x}} & -\frac{1}{m}\hat{d} & -\frac{1}{m}\hat{\beta}\hat{x} + \frac{1}{m} & -\frac{1}{m}\hat{\alpha}\hat{x}e^{\hat{\beta}\hat{x}} & -\frac{1}{m}\hat{\dot{x}} \\ 0 & 0 & 0 & 0 & 0 \\ 0 & 0 & 0 & 0 & 0 \\ 0 & 0 & 0 & 0 & 0 \\ 0 & 0 & 0 & 0 & 0 \end{bmatrix} \tag{4.4}$$

$$G = \begin{bmatrix} 0 & 0 & 0 & 0 \\ \frac{1}{m} & 0 & 0 & 0 \\ 0 & 1 & 0 & 0 \\ 0 & 0 & 1 & 0 \\ 0 & 0 & 0 & 1 \end{bmatrix} \tag{4.5}$$

In the system model, there exists noise in the process that is represented as the process covariance matrix P (Equation 4.6). The diagonal elements of the P matrix are the standard deviation of the state variables in the process. Values of these standard deviation are chosen to be large if the confidence with initial estimates $\hat{\mathbf{x}}(0)$ is low, and small if the confidence is high. In addition to the process covariance, the disturbances (process noise) also exhibits some uncertainties that are reflected in the process noise covariance matrix Q_w (Equation 4.7). Both the process and process noise covariance matrices are chosen to be diagonal. While x and $\dot{x}$ are uncorrelated in the process, we

assume that α, β, and d are uncorrelated among each other as well. In the process noise, all the four parameters are uncorrelated.

$$P = \begin{bmatrix} \sigma_x^2 & 0 & 0 & 0 & 0 \\ 0 & \sigma_{\dot{x}}^2 & 0 & 0 & 0 \\ 0 & 0 & \sigma_\alpha^2 & 0 & 0 \\ 0 & 0 & 0 & \sigma_\beta^2 & 0 \\ 0 & 0 & 0 & 0 & \sigma_d^2 \end{bmatrix} \tag{4.6}$$

$$Qw = \begin{bmatrix} \sigma_{w,u}^2 & 0 & 0 & 0 \\ 0 & \sigma_{w,\alpha}^2 & 0 & 0 \\ 0 & 0 & \sigma_{w,\beta}^2 & 0 \\ 0 & 0 & 0 & \sigma_{w,d}^2 \end{bmatrix} \tag{4.7}$$

As EKF works for discrete-time systems, the continuous-time matrices can be converted into their discrete-time equivalents. The continuous-time state matrix is converted into the discrete-time equivalent as shown in Equation 4.8. dt is the sampling time interval that depends on the system hardware. In the case of this work, dt is equal to the sampling rates set in *LabVIEW* (1 ms). The input matrix is converted into its discrete-time equivalent by taking into account contribution from the process noise covariance matrix, as shown in Equation 4.9.

$$\Phi = e^{Fdt} \tag{4.8}$$

$$Q = GQ_wG^T dt \tag{4.9}$$

In the first stage of the EKF (the time update or prediction), the state variables to be estimated are propagated in time from the estimates at the previous time step. The time updates for the state variables are shown in Equation 4.10. The $-$ notation indicates state variable prior to time update, and the $+$ notation indicates state variable after the time update. During the time update, the process covariance matrix P is also

updated in time as shown in Equation 4.11.

$$\begin{aligned}
\hat{x}(t)^- &= \hat{x}(t-1)^+ + \hat{\dot{x}}(t-1)^+ dt \\
\hat{\dot{x}}(t)^- &= \hat{\dot{x}}(t-1)^+ + \hat{\ddot{x}}(t-1)dt \\
\hat{\ddot{x}}(t-1) &= -\frac{\hat{d}(t-1)}{m}\hat{\dot{x}}(t-1) - \frac{\hat{\alpha}(t-1)}{m}(e^{\hat{\beta}(t-1)\hat{x}(t-1)} - 1) + \frac{1}{m}u(t-1) \\
\hat{\alpha}(t)^- &= \hat{\alpha}(t-1)^+ \\
\hat{\beta}(t)^- &= \hat{\beta}(t-1)^+ \\
\hat{d}(t)^- &= \hat{d}(t-1)^+
\end{aligned} \tag{4.10}$$

$$P(t)^- = \Phi P(t-1)^+ \Phi^T + Q \tag{4.11}$$

4.1.2 Measurement Model

The measurement model comes from the sensor that is attached to the system. In the *smart tool*, there are two variable measured: tissue displacement x using the encoder, and force applied by the motor at the handle u using the strain gages. The measurement equation is shown in Equation 4.12. $\mathbf{y}$ is the output vector which consists of only the displacement x. H is the continuous-time output matrix, as shown in Equation 4.13. Noise in the measurement is considered in this work by having measurement covariance matrix R as depicted in Equation 4.14.

$$\mathbf{y} = H\mathbf{x} + \mathbf{v} \tag{4.12}$$

$$H = \begin{bmatrix} 1 & 0 & 0 & 0 & 0 \end{bmatrix} \tag{4.13}$$

$$R = \sigma_{r,x}^2 \tag{4.14}$$

After the time update, the state variables are corrected in the second stage of EKF (measurement update or correction). In this stage, prediction error is calculated by subtracting estimated data from time update with measurement data from sensor (Equation 4.15. Then, the prediction error is multiplied with the Kalman gain K (Equation 4.17)

before being substracted from the time updates to get final estimated values (Equation 4.18. This process is also called error-state Kalman filtering. Equation 4.16 shows the Kalman gain equation. In the measurement update stage, the process covariance matrix P is also updated as shown in Equation 4.19.

$$dy = \hat{x}(t)^{-} - x(t) \tag{4.15}$$

$$K = P(t)^{-}H^{T}(HP(t)^{-}H^{T} + R)^{-1} \tag{4.16}$$

$$\mathbf{dx} = Kdy \tag{4.17}$$

$$\begin{aligned} \hat{x}(t)^{+} &= \hat{x}(t)^{-} - dx_1 \\ \hat{\dot{x}}(t)^{+} &= \hat{\dot{x}}(t)^{-} - dx_2 \\ \hat{\alpha}(t)^{+} &= \hat{\alpha}(t)^{-} - dx_3 \\ \hat{\beta}(t)^{+} &= \hat{\beta}(t)^{-} - dx_4 \\ \hat{d}(t)^{+} &= \hat{d}(t)^{-} - dx_5 \end{aligned} \tag{4.18}$$

$$P(t)^{+} = (I - KH)P(t)^{-}(I - KH)^{T} + KRK^{T} \tag{4.19}$$

4.2 Verification of the Extended Kalman Filter for Simulation of Tissue Model during Grasping

4.2.1 Simulation of Tissue Model during Grasping

Prior to implementing the EKF into the *Smart Tool* hardware, we performed simulation of EKF with a nonlinear model of tissue during grasping as presented in Equation 4.1 in Section 4.1 earlier. The nonlinear model is created in *SIMULINK* and shown in Figure 4.1.

All parameters used for the simulation are shown in Table 4.1. The mass is selected based on estimation from calculation of tissue volume grasped multiplied by tissue density ($\rho \approx \rho_{water} = 1\text{kg/m}^3$). α and β values for different tissues are adapted from

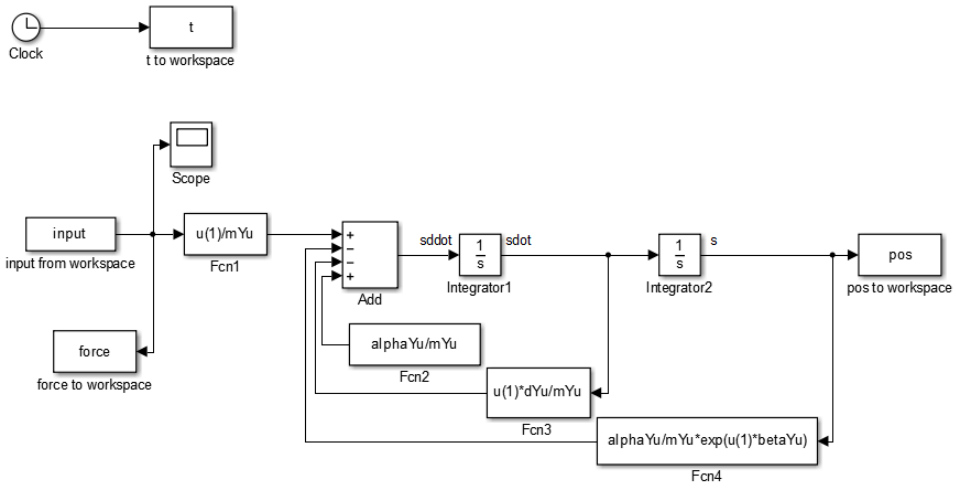

Figure 4.1: *SIMULINK* block diagram of nonlinear model for tissue during grasping

values obtained by Brown et al in [2] for soft tissue model as a basic exponential function ($\sigma = \bar{\alpha}(e^{\bar{\beta}\epsilon} - 1)$). Due to differences in variables used in this work and that of [2], simple conversions of α and β are performed as shown in Equation 4.20, where A_{jaw} is the surface area of grasper jaw and x_0 is initial tissue thickness. Lastly, the tissue damping coefficient values d are approximated at random by applying the minimum values at which the tissue dynamics model became stable.

Table 4.1: Parameters Used for Simulation of Nonlinear Model of Soft Tissue During Grasping

Parameters	Tissue Types			
	Liver	Small Bowel	Bladder	Gallbladder
Mass m (kg)	0.005			
Grasper jaw surface area A_{jaw} (mm^2)	56.3			
Initial tissue thickness x_0 (mm)	7.5	5.5	26	26
$\bar{\alpha}$ (N)	849.2	518.9	0.005	379.3
$\bar{\beta}$ (N and m^{-1})	14.32	11.87	20.46	11.26
Tissue damping coefficient d (kg s^{-1})	3.1	3.3	1.3	0.5
Pressure threshold (kPa)	60	100	40	40

$$\begin{aligned} &\text{Stress-strain relationship in [2]}: \quad \sigma = \bar{\alpha}(e^{\bar{\beta}\epsilon} - 1) \\ &\text{Force-displacement relationship}: \quad F = \alpha(e^{\beta x} - 1) \\ &\sigma = \frac{F}{A_{jaw}} \quad \epsilon = \frac{x - x_0}{x_0} \\ &\alpha = \bar{\alpha}(A_{jaw}) \quad \beta = \frac{\bar{\beta}}{x_0} \end{aligned} \tag{4.20}$$

Input of sinusoidal forces with peak to peak magnitude of 2N (max 2N, min 0N) and frequency of 4Hz is given to the *SIMULINK* model. Maximum input force of 2N is chosen as it was the smallest maximum force that is tolerable among the gastro-intestinal tissues before any injuries could happen [11]. Input frequency of 4Hz is chosen by performing a simple experiment to test the maximum number of grasp a human hand can execute within 1s. However, at the first sinuosial wave is set to be at 2Hz to allow for tissue detection to be completed before a full grasp. The input force to *SIMULINK* for all simulations is shown in Figure 4.2.

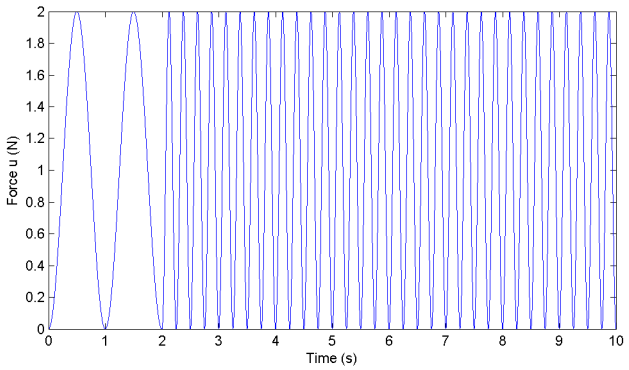

Figure 4.2: Input force for simulation of nonlinear tissue model in *SIMULINK*

Initial conditions for the simulation are set to zero. The simulation solver is set to be the fixed-step ode3 (Bogacki-Shampine) with a fixed sampling time dt of 1ms (0.001s).

Output displacement obtained from the simulation for all tissue types are shown in Figure 4.3. The resulting force and position data from *SIMULINK* are used as the u and x in the EKF respectively.

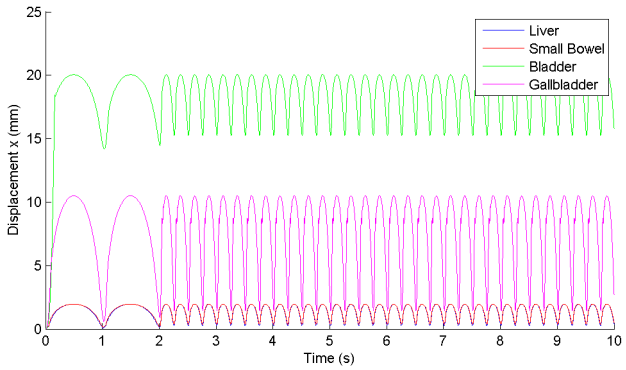

Figure 4.3: Resulting tissue displacements obtained from simulation of nonlinear tissue in *SIMULINK*

4.2.2 EKF Tuning and Results

The EKF is tuned such that values of parameters shown in Table 4.2 are used for all estimation simulations. Initial estimate (guess) for the EKF is set to be equal to Equation 4.21, whereby the values of α, β, and d are obtained for each tissue types from Table 4.1. Furthermore, some random noise is added to the measurement values x and u as uniformly distributed pseudorandom numbers for the EKF analysis to create a more realistic measurement case.

$$\hat{\mathbf{x}}(0) = \begin{bmatrix} x_0 & \dot{x}_0 & \alpha_0 & \beta_0 & d_0 \end{bmatrix}^T = \begin{bmatrix} x & \frac{x(2)-x(1)}{dt} & 0.9\alpha & 0.9\beta & 0.9d \end{bmatrix}^T \tag{4.21}$$

The estimated states values over time (α, β, d, x) for all the four tissues as compared to the actual state values are shown in Figures 4.4(a) - 4.7(a). In addition, Table 4.3 shows the mean of the final estimated states values from ten EKF estimation simulations performed in *MATLAB*.

Figures 4.4(b) - 4.7(b) show the plot of the force equation $F = \alpha(e^{\beta x} - 1)$ using α and β from [2], the force equation using estimated values of $\hat{\alpha}$ and $\hat{\beta}$, the force input to *SIMULINK* u, and the threshold force for the specific tissue type. Also, concatenated below the forces plots, force errors (estimated force subtracted with the force input to *SIMULINK*) are shown. The force error threshold is chosen as 15% of the maximum

Table 4.2: Covariance Matrices for EKF Verification Simulation

Covariance Matrix P	
σ_x	0.01mm
$\sigma_{\dot{x}}$	5mm
σ_α	0.3α
σ_β	0.3β
σ_d	$0.1d$
Process Noise Covariance Matrix Q_w	
$\sigma_{w,u}$	0.5
$\sigma_{w,\alpha}$	0.3α
$\sigma_{w,\beta}$	0.3β
$\sigma_{w,d}$	0.5
Measurement Covariance Matrix R	
$\sigma_{r,x}$	0.01mm

Table 4.3: Steady State Values of Estimated States and Actual States in EKF Verification Simulation

Tissue Type	Estimated States			Actual States		
	$\bar{\hat{\alpha}}$	$\bar{\hat{\beta}}$	$\bar{\hat{d}}$	$\bar{\alpha}$	$\bar{\beta}$	$\bar{d}$
Liver	799.9094	14.5509	4.7069	849.2	14.32	3.1
Small Bowel	489.3628	12.0474	5.014	518.9	11.87	3.3
Bladder	0.0046	20.5933	2.489	0.005	20.46	1.3
Gallbladder	356.6571	11.4143	1.3985	379.3	11.26	0.5

input force value to simulation u.

Figure 4.8 shows the stress versus strain plot of Equation 4.20 calculated using the actual $\bar{\alpha}$ and $\bar{\beta}$ values as well as using steady state estimated $\bar{\hat{\alpha}}$ and $\bar{\hat{\beta}}$ values.

4.2.3 Discussion and Conclusion

It can be seen in Figures 4.4(a) - 4.7(a) that the estimated tissue stiffness parameters $\hat{\alpha}$ and $\hat{\beta}$ converge to steady state values within 0.5s for liver, small bowel, and gallbladder, and 0.25s for bladder. The estimated $\hat{\beta}$ for all tissue types reach steady state values that are closer to the the actual β. Nevertheless, error in estimated $\hat{\alpha}$ as compared to

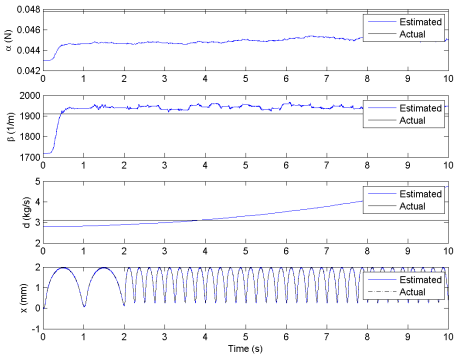

(a) Estimated states

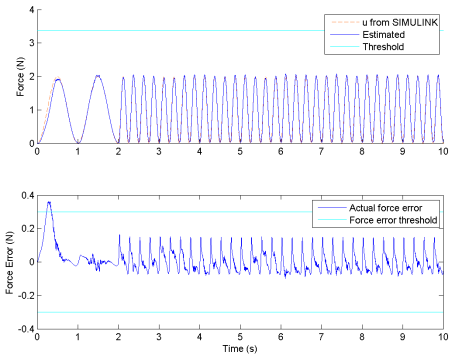

(b) Calculated force with (α,β) and ($\hat{\alpha}$,$\hat{\beta}$), input force to simulation u, and force error

Figure 4.4: Liver simulation results

actual α for all tissue types are larger. The main reason for this is that the state β is directly coupled to the measured state x, allowing for a better estimate of β. On the other hand, the state α is coupled to β and x, causing small error in β to show up as larger error in α. We could see that the tissue damping coefficient d for all tissue types do not converge to a steady state value, rather keep increasing. This fact might suggest that better estimates of α, β, and x could be achieved by having the errors absorbed by the d estimate. The estimated displacement $\hat{x}$ of all the four tissue types are very closely similar to the actual displacement x obtained from the simulation.

From Figures 4.4(b) - 4.7(b), it can be seen that the resulting tissue force calculated using estimated $\hat{\alpha}$ and $\hat{\beta}$ as well as actual α and β start converging with each other with an error of lower than 15% the maximum force after 0.379s for liver, 0.354s for small bowel, 0.282s for bladder, and 0.369s for gallbladder. Thus it can be concluded that the EKF designed is able to perform parameter estimation of tissue stiffness α and β and estimate the correct amount of force delivered to tissue within the first 0.4s in simulation. Within that time frame of grasping a new organ or tissue, it is ideal that a control algorithm is implemented to prevent force applied to tissue to be larger than 2N. Lastly from Figures 4.4(b) - 4.7(b) , it can be concluded that even though the steady state values of estimated $\hat{\alpha}$ are deviating from the actual values, the final estimated force equations are closely similar to the actual force equation. Table 4.4 summarizes

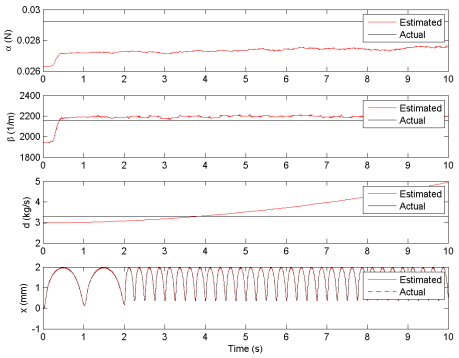

(a) Estimated states

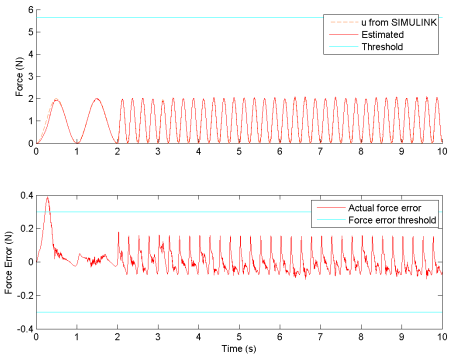

(b) Calculated force with (α,β) and ($\hat{\alpha}$,$\hat{\beta}$), input force to simulation u, and force error

Figure 4.5: Small bowel simulation results

the convergence time for estimated $\hat{\alpha}$ and $\hat{\beta}$ to reach steady states, and also for force error dropping below 15% of the maximum force threshold.

Table 4.4: Convergence Time and Value of Force Error of EKF Verification Simulation

		Tissue Types			
		Liver	Small Bowel	Bladder	Gallbladder
Convergence Time (s)	Max	0.425	0.380	0.292	0.425
	Mean	0.379	0.354	0.282	0.369
	Min	0.346	0.290	0.270	0.334
Force Error (N)	Max	0.405	0.398	0.610	0.413
	Mean	0.014	0.010	0.010	0.013
	Min	-0.167	-0.179	-0.300	-0.242

Finally, it can be seen from Figure 4.8 that the stress-strain curves using estimated values of $\bar{\hat{\alpha}}$ and $\bar{\hat{\beta}}$ coincides with the curves using actual values of $\bar{\alpha}$ and $\bar{\beta}$. This fact verifies that the EKF algorithm developed is able to perform estimation of tissue parameters well thus able to identify different tissue types. In the next section, we will elaborate the algorithm and procedure that is going to be employed for actual tissue identification.

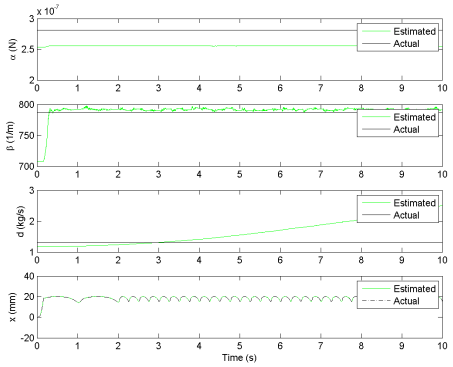

(a) Estimated states

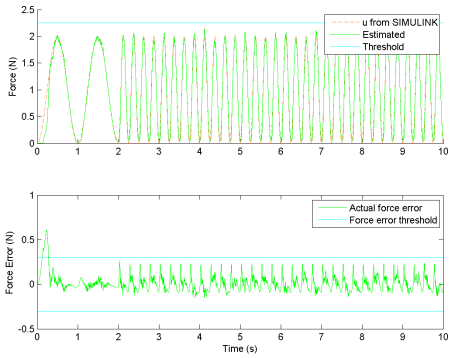

(b) Calculated force with (α,β) and ($\hat{\alpha}$,$\hat{\beta}$), input force to simulation u, and force error

Figure 4.6: Bladder simulation results

4.3 Identification of Tissue Simulation Using Extended Kalman Filter

4.3.1 EKF Tuning and Results

In the previous section, we verify that the EKF algorithm designed is able to perform estimation on tissue parameters related to stiffness (α and β) well. However, the initial guess of those parameters are close to their actual values. In reality, prior information on tissue type being grasped is not available. Thus, we should be able to apply a random initial guess of the parameters and set the covariance matrices large, indicating that confidence on initial guess is low. Eventually, the steady state values of estimated states (parameters) are considerably close to the actual states (parameters). The drawback of this approach is slow convergence rate for estimated parameters, especially $\hat{\alpha}$ and $\hat{\beta}$. Using liver as initial guess tissue as well as modified covariances as shown in Table 4.5, Table 4.6 and 4.7 show the steady state values of estimated parameters, and the convergence time and force error of resulting EKF estimation simulation respectively.

Despite this, it is desired that tissue identification can be performed in the fastest possible time during grasping. In order to evaluate the ability of the EKF algorithm to identify tissue fast, we employ four different initial guesses. The first initial guess would be using α, β, and d for liver tissue. The second would be small bowel tissue, the third

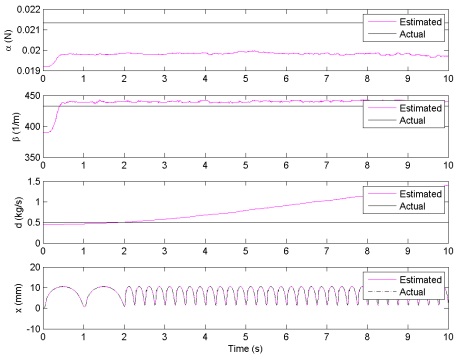

(a) Estimated states

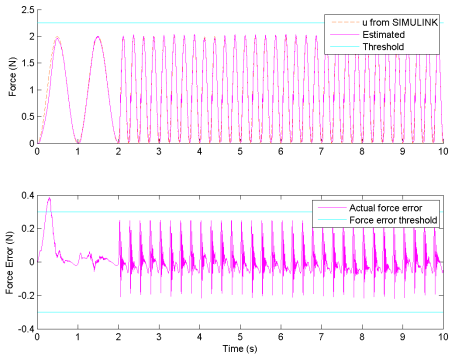

(b) Calculated force with (α,β) and ($\hat{\alpha}$,$\hat{\beta}$), input force to simulation u, and force error

Figure 4.7: Gallbladder simulation results

would be bladder tissue, and the last would be gallbladder tissue. The original "small" covariance matrices from Table 4.2 is used, with the goal of a faster convergence time.

Table 4.8 shows the convergence time for the force error for all four tissue types with EKF implemented using all four different initial conditions. The EKF simulation for each initial tissue guess is ran five times in *MATLAB*.

4.3.2 Discussion and Conclusion

From the table, it can be seen that the absolute value of force error and the convergence time of the force error indicate tissue type being analyzed. Bladder and gallbladder have the fastest convergence time and smallest force error for the correct initial guess tissue. For liver tissue, the convergence time for initial guess of small bowel is fastest, but with slightly larger mean and absolute errors than that of initial guess liver. Meanwhile for small bowel tissue, the convergence time for initial guess of small bowel is the fastest, but with slightly larger mean and absolute errors than that of initial guess liver. This result indicates that tissue identification using EKF algorithm is possible with convergence rate of around 0.4s. Unique identification of bladder and gallbladder can be performed with this method, but additional information has to be analyzed in order to differentiate liver and small bowel.

Figures 4.9(a) - 4.9(d) show the stress-strain plots for all tissue types under all four

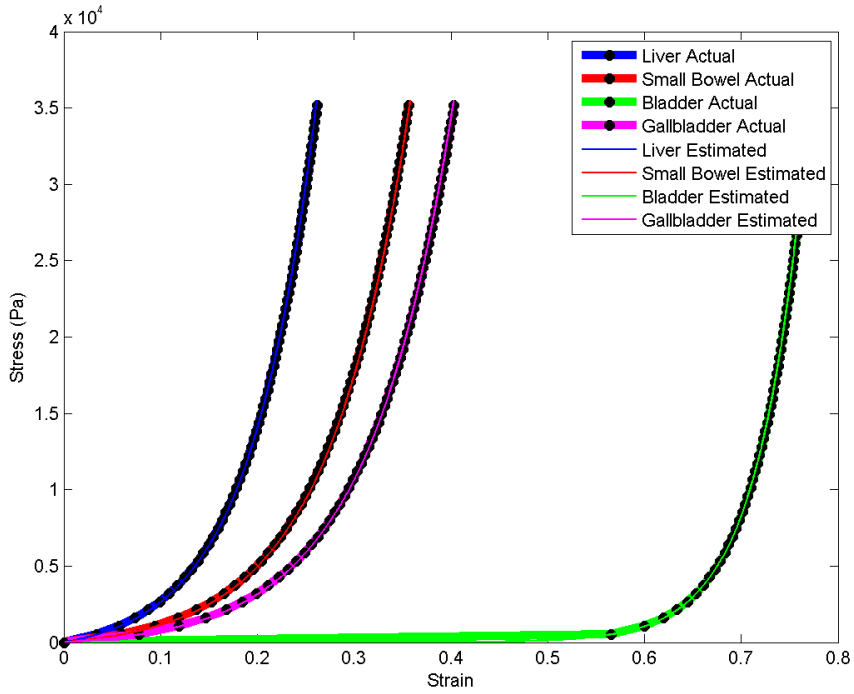

Figure 4.8: Stress-strain plots for various tissue types using $\hat{\alpha}$ and $\hat{\beta}$ estimated from EKF simulation

initial guess tissue. It can be seen from Figure 4.9(a) that although the initial tissue guess is only liver, the EKF algorithm is able to estimate tissue parameters such that the resulting stress-strain relationships among all tissue types are distinct, regardless of the accuracy of the final estimated parameters $\hat{\alpha}$, $\hat{\beta}$, and $\hat{d}$. Also, it can be seen that the final estimated values of $\hat{\hat{\alpha}}$ and $\hat{\hat{\beta}}$ for initial tissue guess of bladder is singular for all tissue types except bladder. Thus, it can be concluded that the initial guess of tissue parameters should not be too far off from the actual tissue parameters to prevent singularity in the EKF estimation.

Table 4.5: Covariance Matrices for Tissue Identification Simulation

Covariance Matrix P	
σ_x	0.01mm
$\sigma_{\dot{x}}$	5mm
σ_α	3α
σ_β	3β
σ_d	$0.1d$
Process Noise Covariance Matrix Q_w	
$\sigma_{w,u}$	0.5
$\sigma_{w,\alpha}$	3α
$\sigma_{w,\beta}$	3β
$\sigma_{w,d}$	0.5
Measurement Covariance Matrix R	
$\sigma_{r,x}$	0.01mm

Table 4.6: Steady State Values of Estimated States and Actual States in Tissue Identification Simulation

Tissue Type	Estimated States			Actual States		
	$\bar{\hat{\alpha}}$	$\bar{\hat{\beta}}$	$\bar{\hat{d}}$	$\bar{\alpha}$	$\bar{\beta}$	$\bar{d}$
Liver	837.811	14.489	4.738	849.2	14.32	3.1
Small Bowel	609.008	11.433	4.767	518.9	11.87	3.3
Bladder	117.2502	6.053	4.404	0.005	20.46	1.3
Gallbladder	539.646	12.174	3.572	379.3	11.26	0.5

4.4 The Recursive Least Squares Estimator

In addition to the Kalman filter algorithm, the recursive least squares (RLS) algorithm is tested and implemented for the tissue model in simulation. A total least squares approach is taken by iterating the total least squares at every time sample, mimicking the recursive least squares while obviating the need for selecting RLS initial values. The least squares estimator is used to estimate tissue parameters α and β that are going to be used to differentiate tissue types.

In order to implement RLS algorithm to the tissue model shown in Equation 4.1, the nonlinear exponential term of the model has to be written in terms of polynomial.

Table 4.7: Convergence Time and Value of Force Error of Tissue Identification Simulation

		Tissue Types			
		Liver	Small Bowel	Bladder	Gallbladder
Convergence Time (s)	Max	6.364	8.840	0.182	0.480
	Mean	4.616	7.648	0.180	0.417
	Min	2.619	4.352	0.177	0.350
Force Error (N)	Max	0.440	0.389	2.425	0.785
	Mean	0.002	-0.001	-0.011	0.016
	Min	-0.412	-0.444	-1.396	-0.865

Equation 4.1 is re-written as a Taylor series expansion about zero (Mclaurin series), as shown in Equation 4.22, which can be further written into a vector form as shown in Equation 4.23.

$$u = m\ddot{x} + d\dot{x} + \frac{\alpha\beta}{1!}x + \frac{\alpha\beta^2}{2!}x^2 + \ldots + \frac{\alpha\beta^n}{n!}x^n \tag{4.22}$$

$$\begin{gathered} u = m\ddot{x} + d\dot{x} + \mathbf{D}\mathbf{\Phi} \\ u = m\ddot{x} + d\dot{x} + \begin{bmatrix} x & \frac{x^2}{2!} & \ldots & \frac{x^n}{n!} \end{bmatrix} \begin{bmatrix} \alpha\beta & \alpha\beta^2 & \ldots & \alpha\beta^n \end{bmatrix}^T \end{gathered} \tag{4.23}$$

The coefficients of the Taylor polynomials $\mathbf{\Phi}$ can be estimated using total least squares algorithm as shown in Equation 4.24, where $u(t)$ and $x(t)$ are the force and displacement of the tissue measured at every time instant. The velocity $\dot{x}(t)$ and acceleration $\ddot{x}(t)$ are obtained by performing noise robust differentiation by Holoborodko [52]. The least squares calculation in Equation 4.24 is performed at every iteration throughout the simulation / measurement.

$$\mathbf{\Phi}(t) = (\mathbf{D}(t)^*\mathbf{D}(t))^{-1}\mathbf{D}(t)^*(u(t) - m\ddot{x}(t) - d\dot{x}(t)) \tag{4.24}$$

After obtaining the estimates of the Taylor polynomials coefficients, the tissue stiffness parameters α and β can be extracted. There are several methods to extract α and β from Taylor coefficients, which are (1) simple division, (2) nonlinear fit to the

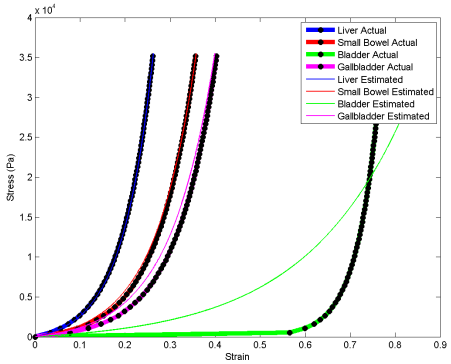

(a) Initial guess tissue liver

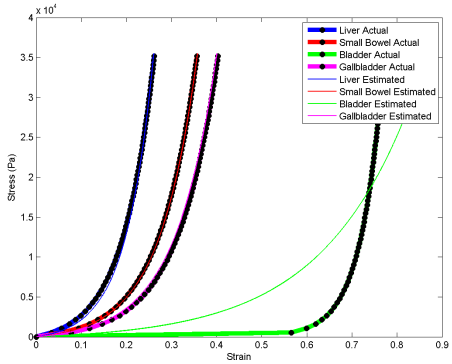

(b) Initial guess tissue small bowel

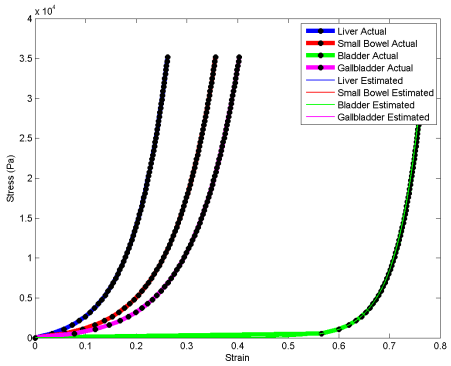

(c) Initial guess tissue bladder

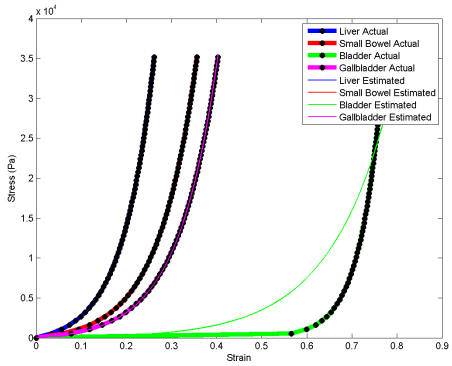

(d) Initial guess tissue gallbladder

Figure 4.9: Stress-strain plots for various tissue types using four different initial guess tissue

exponential function $\alpha(e^{\beta x}-1)$, (3) closed form solutions of α and β from error function between actual and estimated force function.

The first method of extracting α and β is by simple division as shown in Equation 4.25. It is observed that simple division is capable of extracting α and β well if there is no noise present in the measurement. However, if there is noise in the measurement, which is typical in real *in vivo* measurement data, simple division will amplify the noise

and fail to estimate α and β correctly.

$$\begin{aligned} \alpha &= \frac{\mathbf{\Phi}(1,t)^2}{\mathbf{\Phi}(2,t)} = \frac{(\alpha\beta)^2}{\alpha\beta^2} \\ \beta &= \frac{\mathbf{\Phi}(2,t)}{\mathbf{\Phi}(1,t)} = \frac{\alpha\beta^2}{\alpha\beta} \end{aligned} \tag{4.25}$$

The second method of extracting α and β is by performing a nonlinear fit in *MATLAB*. The nonlinear fit depends largely on initial conditions and is computationally expensive. While the nonlinear fit may be a good choice of extracting α and β from the Taylor coefficients in an offline estimation, the computational time makes it impossible to be implemented in real time with and update rate of 1kHz.

The third method of extracting α and β is performed by obtaining the closed form solutions of α and β in terms of the Taylor polynomial coefficients. They are obtained by taking the derivative of error between estimated and actual taylor polynomial coefficients and solve for α and β. A closed form solution for α exists, but β is not able to be derived as a closed form solution. This results in the need to find a numerical solution (roots) of a high order polynomial in β for every time instant, which may be feasible, but not ideal.

4.4.1 RLS Estimator Tuning and Results

RLS estimations of tissue parameters are performed for simulation of tissue models during grasping for liver, small bowel, bladder, and gallbladder tissue models. The tissue simulations are described in Section 4.2.1. Noise is added to the measurement data x and u obtained from simulation. The velocity and acceleration are obtained by noise robust differentiation of x subsequently. The Taylor series expansion is chosen about zero and up to the order five.

The estimated $\hat{\alpha}$ and $\hat{\beta}$ are extracted by performing a nonlinear fit to the Taylor polynomials.

Figures 4.10(a) to 4.13(b) show the plots of original measured force-displacement plots together with the Taylor polynomials and the plots of estimated $\hat{\alpha}$ and $\hat{\beta}$ parameters together with the actual α and β.

4.4.2 Discussion and Conclusion

From Figures 4.10(a), 4.11(a), 4.12, and 4.13(a), it can be seen that the estimated Taylor polynomials for all tissue types fit the actual force-displacement curves well.

Also, from Figures 4.10(b), 4.11(b), and 4.13(b), it can be seen that the nonlinear fit is able to extract α and β of liver, small bowel, and gallbladder well. The RLS estimator is able to perform estimation within 0.4s. Nevertheless, the estimated values of α and β became large and unstable after 2s. As force application in real time surgery, estimates of tissue parameters are essential during the early stage of grasping, the RLS estimator should be refreshed after every grasp thus will not reach the "unstable" stage.

While the nonlinear fit is able to extract $\hat{\alpha}$ and $\hat{\beta}$ for liver, small bowel, and gallbladder, it fails to extract the values of $\hat{\alpha}$ and $\hat{\beta}$ for bladder.

From the results of the RLS estimation, we can conclude that the RLS estimator is able to perform estimation of Taylor polynomials that fit the actual measured force-displacement profile closely. However, extracting the α and β tissue parameters from the estimated Taylor polynomial coefficients is a challenge.

The RLS estimator provides an alternative to the EKF on tissue differentiation that is independent of initial tissue guess. Nevertheless, the RLS estimator is unable to estimate the measured states, which are force and displacement, that are essential for developing a force control algorithm that regulates force delivered to the tissue.

Table 4.8: Convergence Time and Force Error for Simulation of Tissue Models with Four Different Initial Estimate of Parameters

Initial Guess Tissue			Tissue Grasped: Liver	Small Bowel	Bladder	Gall-bladder
Liver	Convergence Time (s)	Max	0.402	0.400	1.245	9.367
		Mean	0.366	0.384	1.217	6.807
		Min	0.342	0.367	1.196	3.616
	Force Error (N)	Max	0.375	0.393	0.963	0.379
		Mean	0.012	-0.008	-0.121	-0.045
		Min	-0.118	-0.136	-5.210	-3.581
Small Bowel	Convergence Time (s)	Max	0.377	0.367	1.220	8.599
		Mean	0.339	0.359	1.047	4.621
		Min	0.305	0.346	0.423	1.220
	Force Error (N)	Max	0.418	0.409	0.820	0.350
		Mean	0.034	0.011	-0.113	-0.032
		Min	-0.179	-0.120	-5.377	-3.509
Bladder	Convergence Time (s)	Max	8.220	8.470	0.284	2.470
		Mean	8.220	8.220	0.274	2.470
		Min	8.220	7.970	0.259	2.470
	Force Error (N)	Max	2	2	0.632	2
		Mean	∞	∞	0.008	∞
		Min	∞	∞	-0.231	∞
Gallbladder	Convergence Time (s)	Max	9.209	9.217	1.456	0.403
		Mean	9.016	9.032	1.429	0.371
		Min	8.968	8.968	1.397	0.349
	Force Error (N)	Max	1.977	1.977	0.716	0.409
		Mean	1	1	-0.134	0.013
		Min	-0.008	-0.033	-3.251	-0.231

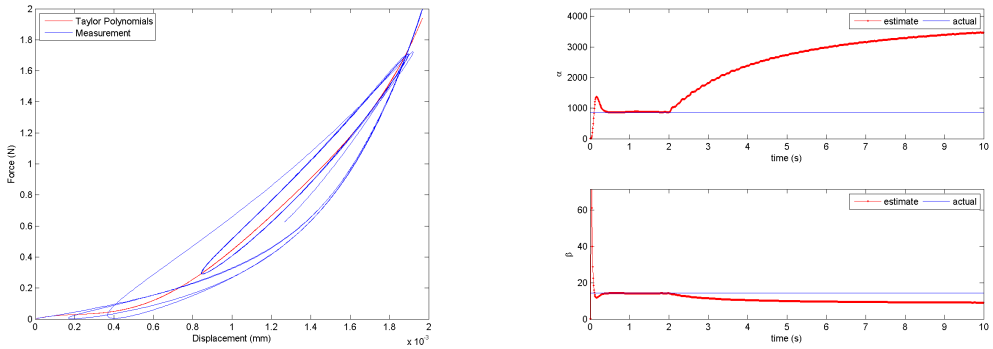

(a) Force-displacement (b) α and β

Figure 4.10: Plots of the actual and estimated force-displacement curve and α, β for liver

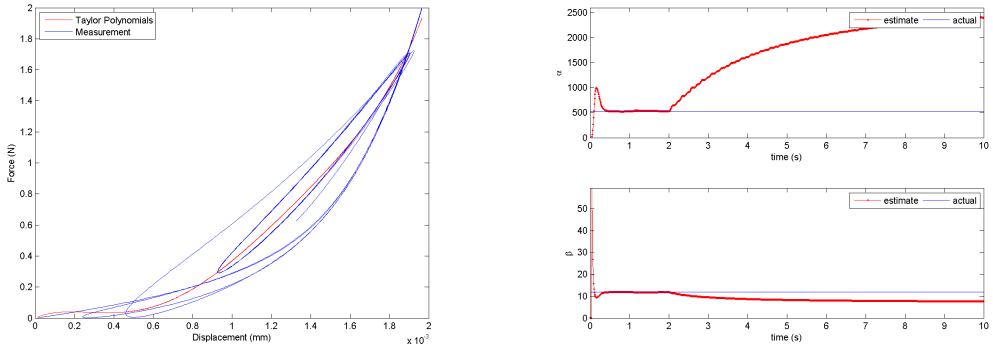

(a) Force-displacement (b) α and β

Figure 4.11: Plots of the actual and estimated force-displacement curve and α, β for small bowel

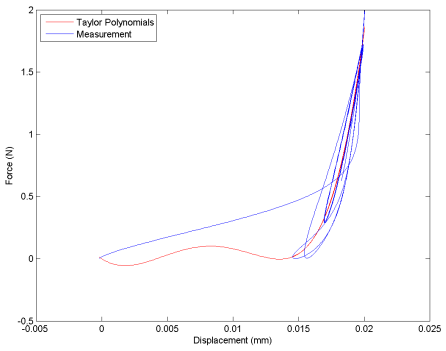

Figure 4.12: Plots of the actual and estimated force-displacement curve for bladder

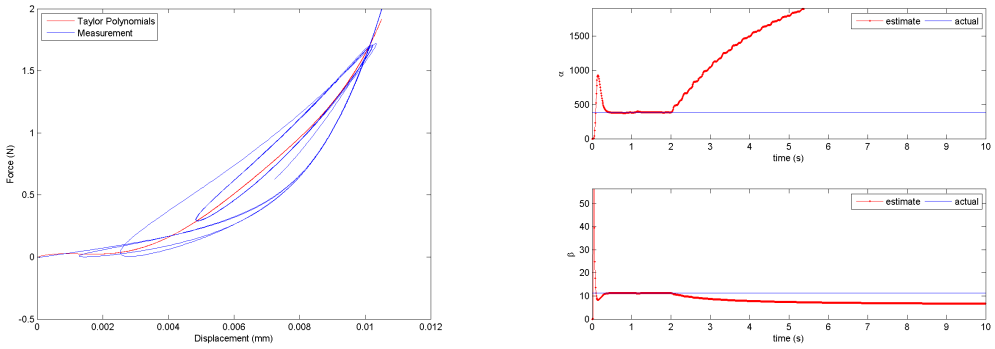

(a) Force-displacement

(b) α and β

Figure 4.13: Plots of the actual and estimated force-displacement curve and α, β for gallbladder

Chapter 5

Identification of *In Vivo* and *In Situ* Porcine Tissues Using Extended Kalman Filter

After verifying the designed EKF algorithm using simulation of tissue model during grasping, we implemented the EKF algorithm on *in vivo* and *in situ* tissue data of two porcine models. Ideally, it is aimed to have the EKF algorithm implemented in *LabVIEW* to perform tissue identification in real time. However, in this work, the identification will be performed offline, using real data collected from tissue.

5.1 Pre-Experimental Protocol and Setup

Prior to collecting experimental data from the porcine models, the developed *Smart Tool* is used to collect force and displacement data of hand tissue to simulate actual porcine tissues *in situ*.

5.1.1 Setting Input Voltage to Motor

Several motor input voltage trajectories are considered, such as sinusoidal, triangle, square, and trapezoidal waveforms. In the tissue simulation, sinusoidal force inputs are given to the tissue. However, it is decided to have trapezoidal voltage waveforms sent

to the motor. The trapezoidal waveform is selected as it mimics real human grasping pattern better as compared to the other three waveform types. First of all the voltage is ramped up from 0V to a certain maximum amplitude, then kept constant, and ramped down to 0V, each three in the same amount of time period. Then, the voltage is kept low at 0V for a longer time period depending on the frequency set. The purpose of keeping the voltage at 0V for a longer time period is to allow for the grasper to fully disengage from tissue, allowing a new "contact" at each grasp.

For data collection in this work, we select three different grasping frequencies to be applied to the tissue: 0.25Hz, 2Hz, and 4Hz. 0.25Hz is selected to simulate a "less frequent" grasping motion, allowing more time of contact between grasper jaws and tissue. 2Hz and 4Hz are selected based on the average and the fastest grasped velocity that can be performed by a surgeon during a surgery. This was tested by counting the number of grasps that can be performed as fast as possible in 10s, and averaging the number of grasps per second for all trials. The test leads to an average of 4 grasps per second (4Hz). In the 0.25Hz grasp, it takes 1s for the force applied at the handle to reach its maximum value from 0. In the 2Hz grasp, the time taken is 120ms, while in the 4Hz grasp, the time taken is reduced to 60ms. Figure 5.1 shows the motor input voltage for the 0.25Hz, 2Hz, and 4Hz grasps.

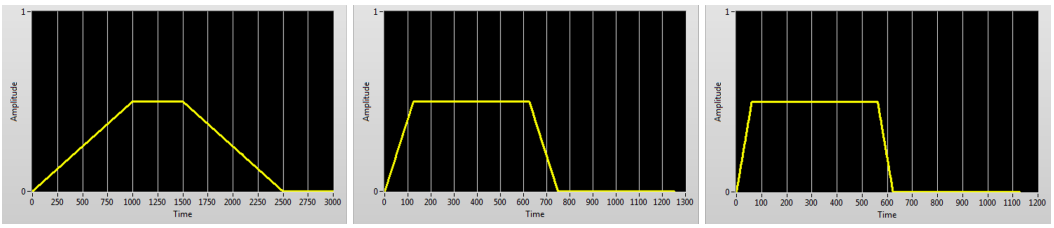

Figure 5.1: Trapezoidal voltage profile output to the motor at 0.25Hz (left), 2Hz (middle), and 4Hz (right) frequencies

Lastly, the maximum motor voltage magnitude is selected based on the lowest force threshold that may lead to tissue injuries for gastrointestinal tissues. The tissue that has the lowest force threshold before injury is ureter with a force threshold of 2.2N [11]. It is desirable to have a maximum of 2N force at the grasper jaws. Based on the motor voltage to strain gage force and tissue force at grasper jaw relationship, it is

obtained that 2V of motor voltage is equivalent to 1.55N of force at the tissue. For the experiment, we select 0.5V (equivalent to 0.8N) and 2V (equivalent to 1.55N) as the maximum amplitude of the trapezoidal motor input signal.

5.1.2 Test Grasping on Hand Tissue

For each grasping session, user is able to select the maximum grasp command amplitude, the grasp frequency, and total number of grasps per session (total number of loop iteration). In the hand tissue grasping session, we select the maximum command amplitude of 0.5V (0.8N) and perform all three grasp frequencies.

At the beginning of each grasping, the encoder is re-zeroed by aligning the partial pulley into the position that makes the grasper jaws fully opened. The grasper jaws are placed such that tissue is in between the jaws. Then, the *LabVIEW* GUI is ran for 20 grasps.

Figure 5.2 shows the resulting analog outputs (strain gage voltage, right and left touch sensors, actual motor voltage received) and digital outputs / counter (encoder) values obtained by the PCI6230 in *LabVIEW*. It can be seen from the figure that there is a lag between the time when input voltage is given to the motor and output voltages are generated by the sensors. The lag is a constant time shift thus do not affect the system behavior. It could be seen that the strain gage voltage and encoder readings are in sync, and the right and left touch sensors are able to detect contact by showing a high 5V signal when in contact with hand tissue.

5.2 Experimental Protocol and Setup

5.2.1 Data Collection on Porcine Models

Data collection on porcine models are performed in the Visible Heart Laboratory at the University of Minnesota. The *Smart Tool*, MSEG circuit board, PCI6230, computer, and monitor are transferred to a mobile workstation and brought into the lab. Two porcine models are used for data collection on two different days. In the first porcine model, data collection is performed for liver *in vivo*. Afterwards, in both porcine models, the heart has been extracted and data collections are performed within 1 hour after the

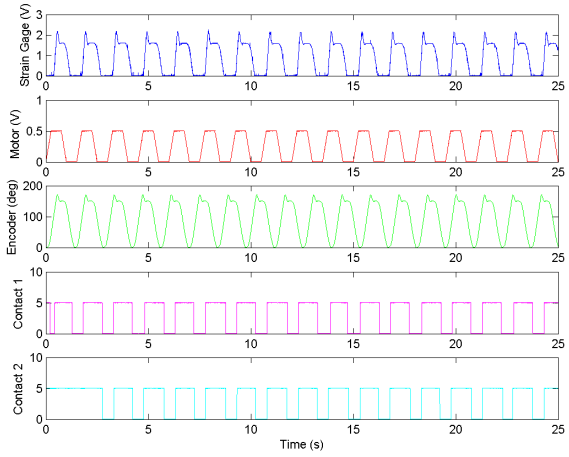

Figure 5.2: Sensor outputs and motor command for hand tissue grasping

heart extraction. The abdomen of both models are cut open, allowing access to organs *in situ*. Figure 5.3 shows the abdomen of the pig that has been cut open. The same data collection procedure is used for grasping session in the porcine models as in the hand tissue test. Grasping sessions are performed for liver, small bowel, gallbladder and bladder in the same order for both porcine models.

During the first data collection from the first porcine model, for each tissue types, we apply two 2Hz 0.5V (0.8N) grasping sessions, followed by two 4Hz 0.5V (0.8N) grasping sessions. The 2Hz grasping sessions consist of 20 grasps and the 4Hz sessions consist of 25 grasps. The exceptions are for liver and gallbladder. For the liver in which two 2Hz 0.5V (0.8N) and one 4Hz 0.5V (0.8N) grasping sessions are performed *in vivo*, and two 2Hz 0.5V (0.8N) and two 4Hz 0.5V (0.8N) grasping sessions are performed *in situ*. For the gallbladder, only one 2Hz 0.5V (0.8N) grasping session and one 4Hz 0.5V (0.8N) grasping session are performed. Each new grasping session is performed at new spots on the tissue. After each grasping session, the encoder is re-zeroed.

The first data collection provided several observations. First, with grasping frequencies as fast as 2Hz and 4Hz, the grasper jaws do not have a chance of leaving contact with tissues, keeping the tissue to be constantly in contact with grasper jaws for each

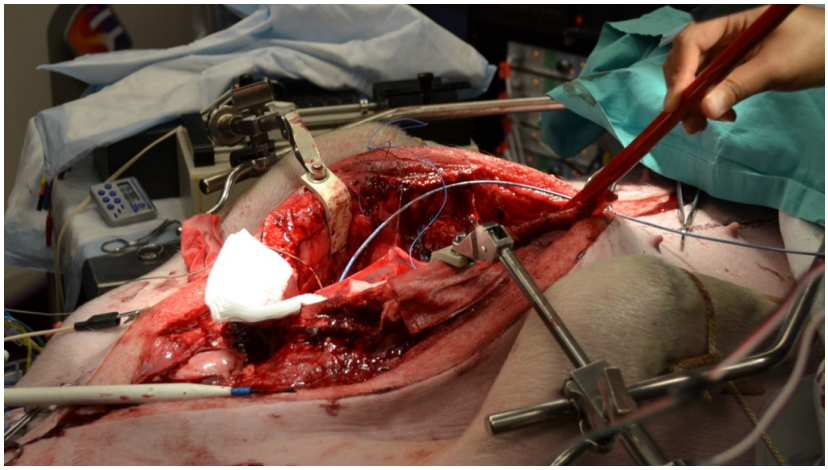

Figure 5.3: Abdomen of pig that has been cut open

grasping session. Secondly, the touch sensors fail to reliably detect contact with tissue. This happens after the grasper jaws come into contact with tissue and blood / tissue liquid seeps in between the wire cable connected to the touch sensor and the jaws teeth.

During the second data collection from the second porcine model, for all tissue types, we apply two 0.25Hz 2V (1.55N) grasping sessions, followed by two 2Hz 2V (1.55N) grasping sessions. The 0.25Hz grasping sessions consist of 10 grasps and the 2Hz grasping sessions consist of 20 grasps. The fact that tissue never leaves contact from grasper jaws during the first data collection motivates us to perform slower grasping sessions, enabling grasper jaws to fully disengage from tissue at every grasp in one grasping session. Similar to the first data collection, each grasping session is performed at a new location on the tissue. The encoder and the touch sensors are reset after each session. Grasping session for ureter is also performed after removing all gastrointestinal organs that block access to the tissue.

Figure 5.4 shows the *Smart Tool* performing the grasping session. Figure 5.5 shows the liver, small bowel, bladder, and gallbladder tissues being grasped by the *Smart Tool*.

Figure 5.4: Setup of a grasping session

5.2.2 Analysis of Raw Data

All collected data during both experiments (analog and digital output values from PCI6230) are recorded via the GUI in *LabVIEW* and stored as *.lvm* files. The log files are imported to *MATLAB* where the EKF algorithm designed is used to perform tissue parameter estimations on the log data. Figure 5.6 shows the plot of sample of all raw data in one grasping session from *LabVIEW*.

The strain gage reading is calibrated to get force values delivered to the tissue at the grasper jaws using Equations 3.2 and 3.8. The final calibrated force value F_{jaw} is used as u in the EKF analysis in *MATLAB*. After performing the force calibration, data from one grasping session is parsed as single grasping during the session. Ideally, the touch sensor is used to determine the time instant when the grasper jaws come into contact with tissue (grasping) and release contact from tissue (releasing). However, the touch sensors fail to provide such information. Thus, the starting of a new grasp is defined as the time instant when the force delivered to the tissue F_{jaw} has gone from below 0.015N to above 0.015N.

Next, the encoder reading is converted into jaw opening using Equations 3.10, 3.11, and 3.15. Tissue initial thickness x_{init} is selected as the first value of jaw opening d_{jaw}. Then, tissue displacement is calculated by subtracting the following jaw opening d_{jaw}

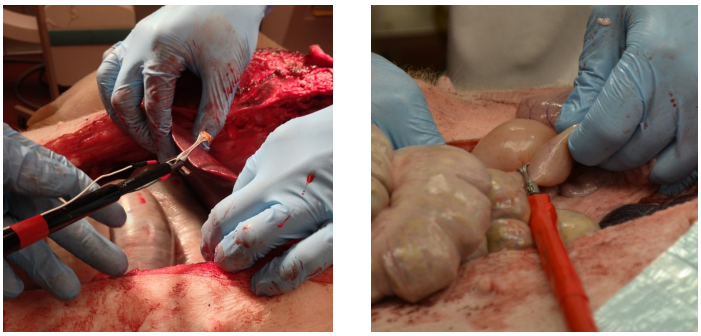

(a) Liver (b) Small Bowel

(c) Bladder (d) Gallbladder

Figure 5.5: Grasping session performed on *in situ* organs

from the initial tissue thickness x_{init}. The tissue displacement calculated is used as x in the EKF analysis in *MATLAB*.

Figure 5.7 shows the plot of force at the tissue F_{jaw}, tissue displacement x, and tissue initial thickness x_{init} for a sample of one single grasp. In the next step, EKF algorithm is implemented for data of each single grasp. That is, for every single grasp, an EKF estimation algorithm is implemented and refreshed. Details on EKF implementation is elaborated in the next section.

A summary of all experimental conditions is shown in Table 5.1.

5.3 EKF Implementation and Results

After processing the raw data obtained from *LabVIEW*, the EKF algorithm designed in Chapter 4 is implemented to the data. Tissue parameters used for the EKF algorithm

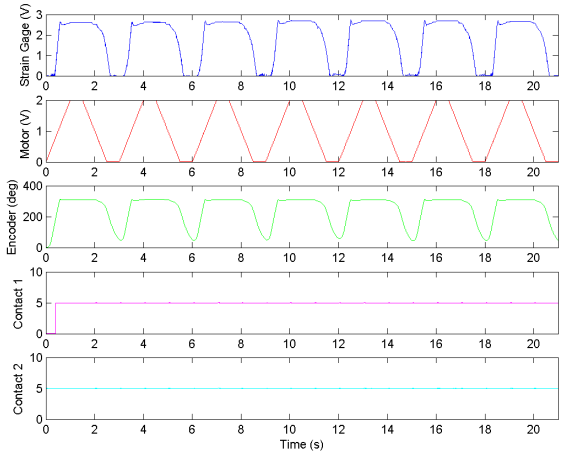

Figure 5.6: Raw sensor outputs and motor command for one porcine tissue grasping session

is shown in Table 5.2. The values of "actual" tissue α and β are the values estimated in the EKF implementation on simulation of tissue during grasping (Chapter 4 Table 4.3). The standard deviation used for the covariance matrices are adjusted from Table 4.2 for the *in vivo* and *in situ* porcine tissue data. The resulting tuned values are shown in Table 5.3. Lastly, the initial estimate (guess) for the EKF is shown in Equation 5.1. All values of α, β, and d used in the covariance matrices and initial estimate are the values corresponding to the respective tissue types being grasped and identified.

$$\hat{\mathbf{x}}(0) = \begin{bmatrix} x & \frac{x(2)-x(1)}{dt} & 0.95\alpha & 0.95\beta & 0.9d \end{bmatrix} \tag{5.1}$$

For each grasp, the EKF algorithm with parameters above are implemented. The resulting estimated state values ($\hat{\alpha}$, $\hat{\beta}$, $\hat{d}$, $\hat{x}$), and estimated force calculated using Equation 4.20 are stored and plotted. Figure 5.8 shows the sample plot of estimated states together with the actual states over time for one single grasp with 0.25Hz frequency and 2V (1.55N) motor command on liver tissue. The force error between the measured force and calculated force using estimated states are computed to find the convergence time of the filter. The convergence time is defined as the latest time instant when the force error drops below and never exceed the error threshold. The error threshold is

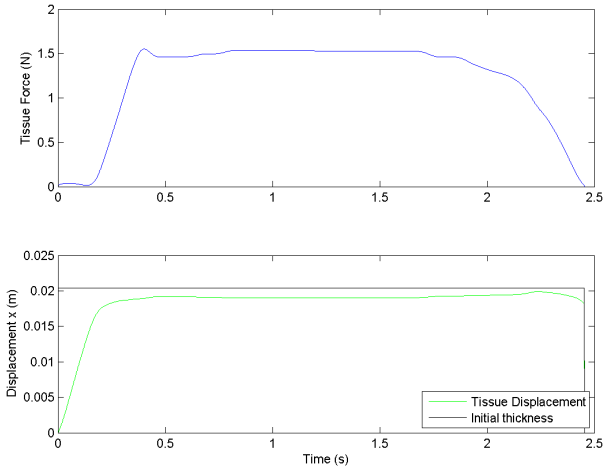

Figure 5.7: Calibrated force delivered to the tissue, tissue displacement, and initial thickness plots for one single grasp

defined as 15% of the maximum force threshold for each tissue type (Table 5.2), same as in simulation. Figure 5.9 shows the plot of measured and estimated force values, and the corresponding force error and error threshold over time for one single grasp with 0.25Hz frequency and 2V (1.55N) motor command on liver tissue. Table 5.4 shows the maximum, mean, and minimum values of convergence time and force error for all tissue types.

Finally, the final or steady state estimated values of $\hat{\tilde{\alpha}}$, $\hat{\tilde{\beta}}$, and $\hat{d}$ for every single grasp is tabulated and plotted in the form of boxplots as shown in Figures 5.10 - 5.12. The mean of steady state $\hat{\tilde{\alpha}}$, $\hat{\tilde{\beta}}$, and $\hat{d}$ for each type of tissue is shown in Table 5.5.

5.4 Discussion and Conclusion

The significance of knowing the force error values over time or the convergence time is to ensure tissue safety, that is, before applying a force that exceeds the maximum value the tissue can tolerate, the force estimation from EKF has converged and we are able to correct force amount delivered to the tissue by applying a control law. We can see

Table 5.1: Tissue Parameters for EKF Implementation on Porcine Tissue Data

Grasp Condition		Tissue Types				
Tissue Force (N)	Grasp Rate (ms)	Liver	Small Bowel	Bladder	Gallbladder	Total
0.8N	120	126	29	50	30	235
	60	91	70	61	30	252
1.55N	1000	20	17	17	14	68
	60	34	39	45	38	156
Total		271	155	173	112	711

Table 5.2: Tissue Parameters for EKF Implementation on Porcine Tissue Identification

Parameters	Tissue Types			
	Liver	Small Bowel	Bladder	Gallbladder
Mass m (kg)	0.005			
$\bar{\alpha}$ (N)	799.9094	489.3628	0.0046	356.6571
$\bar{\beta}$ (N and m^{-1})	14.5509	12.0474	20.5933	11.4143
Tissue damping d (kg s^{-1})	3.1	3.3	1.3	0.5
Pressure threshold (kPa)	60	100	40	40

from Table 5.4 that the force error drops below 15% of the maximum force threshold for each tissue below 0.3s. From Figure 5.1, it can be seen that for the first 0.3s, the 0.25Hz grasp has not reached the its maximum value (grasp has not been completed). Thus, if grasping is performed at a rate of 0.25Hz, force estimation is able to be performed with acceptable accuracy before the grasp is completed.

From Table 5.5, we can see that the EKF algorithm is able to estimate $\hat{\bar{\alpha}}$ and d closely to the actual values for all four tissue types, while the estimates of $\hat{\bar{\beta}}$ are less accurate from the actual values.

As the force error indicates the boundary for keeping the tissue safe, the estimated states ($\hat{\bar{\alpha}}$, $\hat{\bar{\beta}}$, and $\hat{d}$) are important for discriminating tissue types, that is essential before a force control algorithm can be implemented to maintain actual force amount delivered to the tissue. As we can see from Figures 5.10 - 5.12, there are distinct separations for the estimated values of $\hat{\bar{\alpha}}$ and $\hat{d}$ among the four tissue types. Distinct values of estimated $\hat{\bar{\beta}}$ can be observed for bladder and gallbladder, but some overlapping can be seen between

Table 5.3: System, Noise, and Measurement Covariance Matrices for EKF Implementation on Porcine Tissue Identification

Covariance Matrix P	
σ_x	0.01mm
$\sigma_{\dot{x}}$	0.01mm
σ_α	0.05α
σ_β	0.05β
σ_d	$0.01d$
Process Noise Covariance Matrix Q_w	
$\sigma_{w,u}$	0.8
$\sigma_{w,\alpha}$	0.05α
$\sigma_{w,\beta}$	0.05β
$\sigma_{w,d}$	$0.01d$
Measurement Covariance Matrix R	
$\sigma_{r,x}$	0.01mm

liver and small bowel.

We perform a multicomparison test in *MATLAB* on the estimated values of $\hat{\bar{\alpha}}$, $\hat{\bar{\beta}}$, and $\hat{d}$ for all the tissue types. Figures 5.13, 5.14, and 5.15 show the result of the multicomparison test on $\hat{\bar{\alpha}}$, $\hat{\bar{\beta}}$, and $\hat{d}$. Using the estimated values of $\hat{\bar{\alpha}}$, we are able to differentiate the four tissue types. Meanwhile, the resulting estimated values of $\hat{\bar{\beta}}$ are unique for small bowel, bladder, and either liver or gallbladder. Using $\hat{\bar{\beta}}$ information only, the EKF algorithm is not able to differentiate liver from small bowel. From Figure 5.15, we can see that the multicomparison test for estimated $\hat{d}$ are unique for all tissue types. Thus, by using the combination of estimated results of $\hat{\bar{\alpha}}$, $\hat{\bar{\beta}}$, or $\hat{d}$, the EKF algorithm is able to perform tissue identification on *in vivo* and *in situ* porcine tissues.

5.5 RLS Implementation, Results, and Conclusion

We implement the RLS estimator algorithm developed in Chapter 4 to the *in vivo* measurement data. The order of the Taylor series expansion is selected to be ten. In order to have a close fit between the force-displacement curve of the Taylor polynomials and the measurement, the Taylor series expansion has to have an order of six and larger.

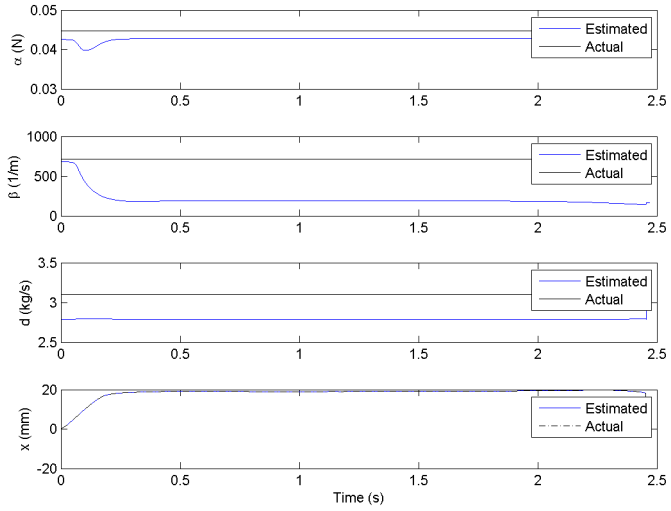

Figure 5.8: Estimated and actual states for 0.25Hz, 2V (1.55N) single grasp on liver tissue

Figure 5.16 shows a sample of the force-displacement curve for 0.25Hz, 2V (1.55N) single grasp on liver tissue. From the figure, it can be seen that the RLS estimator is able to estimate a Taylor polynomial that closely fits the actual force-displacement curve from the measured x and u data.

Extracting the tissue parameters α and β is a challenge. Similarly, the Taylor coefficients estimated for different tissue types are not unique and could not be used to indicate or differentiate specific tissue types. Therefore, even though the RLS estimator is able to perform good estimation on the force-displacement curve, without a robust method of extracting the tissue parameters, it is not a good choice for algorithm to identify tissue types.

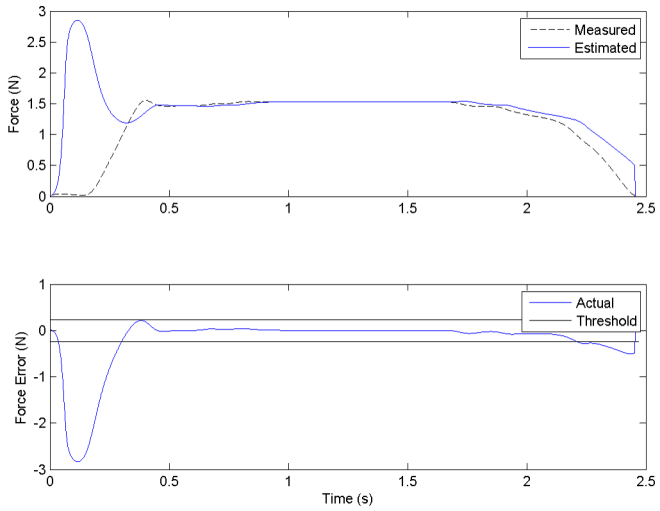

Figure 5.9: Estimated and actual force, force error and error threshold for 0.25Hz, 2V (1.55N) single grasp on liver tissue

Table 5.4: Convergence Time and Force Error for Porcine Tissues Identification

		Liver	Small Bowel	Bladder	Gallbladder
Convergence Time (s)	Max	0.727	0.768	2.419	0.714
	Mean	0.257	0.292	0.309	0.253
	Min	0.029	0.029	0.033	0.073
Force Error (N)	Max	0.679	0.470	0.965	0.668
	Mean	-0.273	-0.276	0.175	-0.177
	Min	-5.304	-1.953	-0.922	-9.325

Table 5.5: Steady State Values of Estimated States and Actual States for Porcine Tissues Identification

Tissue Type	Estimated States			Actual States		
	$\bar{\hat{\alpha}}$	$\bar{\hat{\beta}}$	$\bar{\hat{d}}$	$\bar{\alpha}$	$\bar{\beta}$	$\bar{d}$
Liver	757.8079	5.7578	2.8413	799.9094	14.5509	3.1
Small Bowel	459.1573	4.3212	3.0041	489.3628	12.0474	3.3
Bladder	0.0044	16.9556	1.2132	0.0046	20.5933	1.3
Gallbladder	336.1857	6.4113	0.4554	356.6571	11.4143	0.5

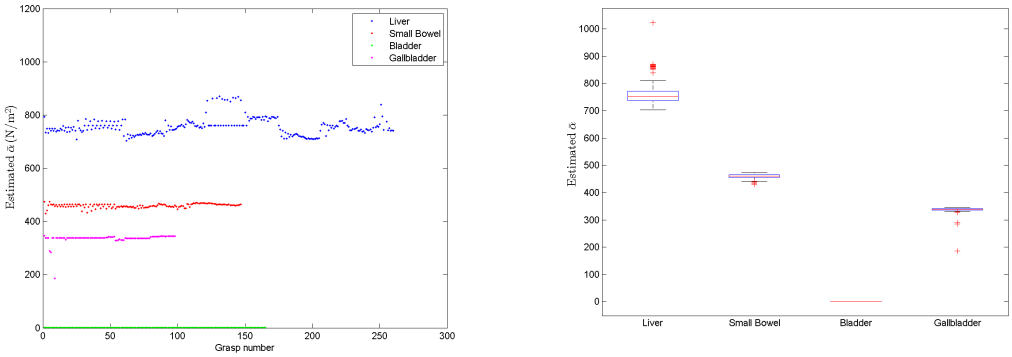

(a) Steady state values (b) Boxplot

Figure 5.10: Plot of steady state values of estimated $\hat{\alpha}$ and boxplot for all grasps on all four tissue types

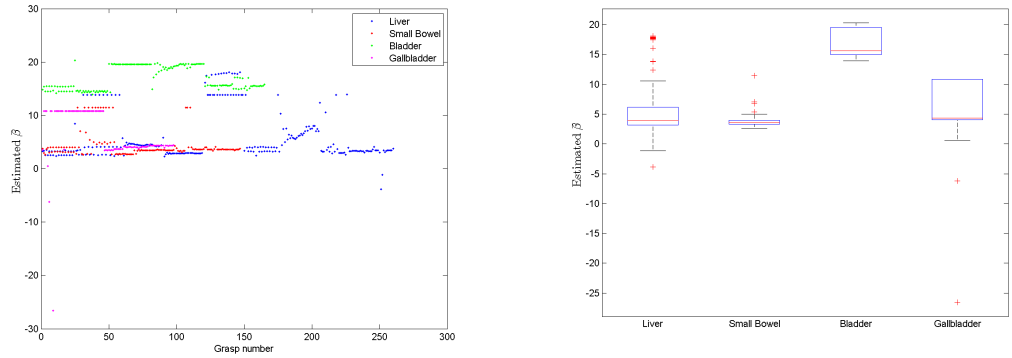

(a) Steady state values (b) Boxplot

Figure 5.11: Plot of steady state values of estimated $\hat{\beta}$ and boxplot for all grasps on all four tissue types

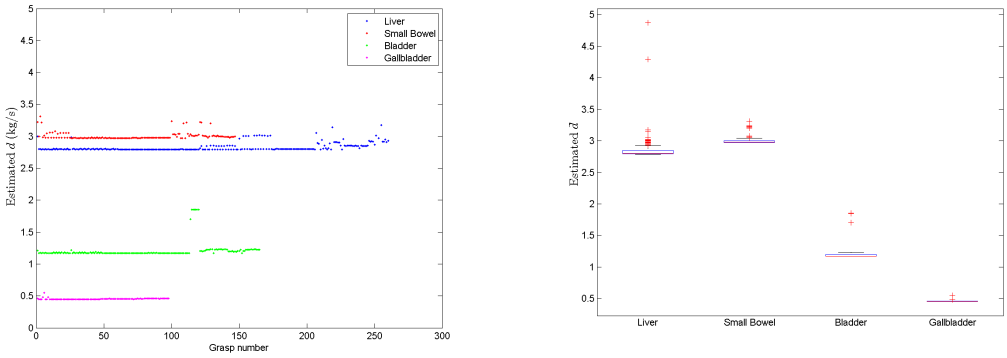

(a) Steady state values

(b) Boxplot

Figure 5.12: Plot of steady state values of estimated $\hat{d}$ and boxplot for all grasps on all four tissue types

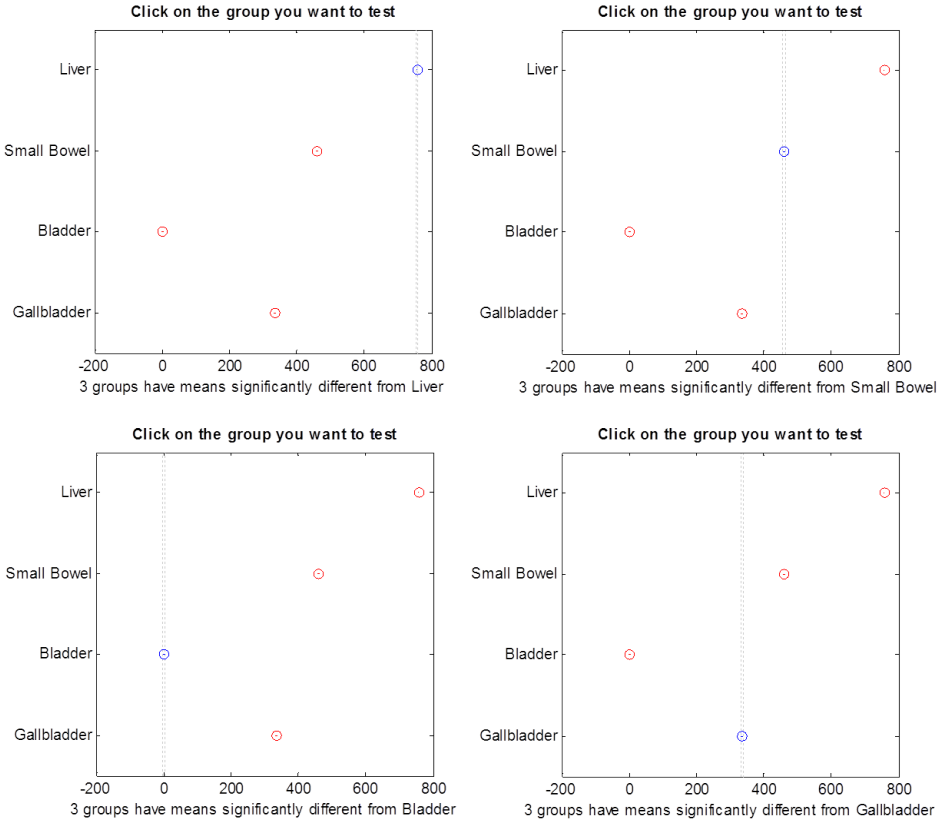

Figure 5.13: *MATLAB* multicomparison results of $\hat{\tilde{\alpha}}$

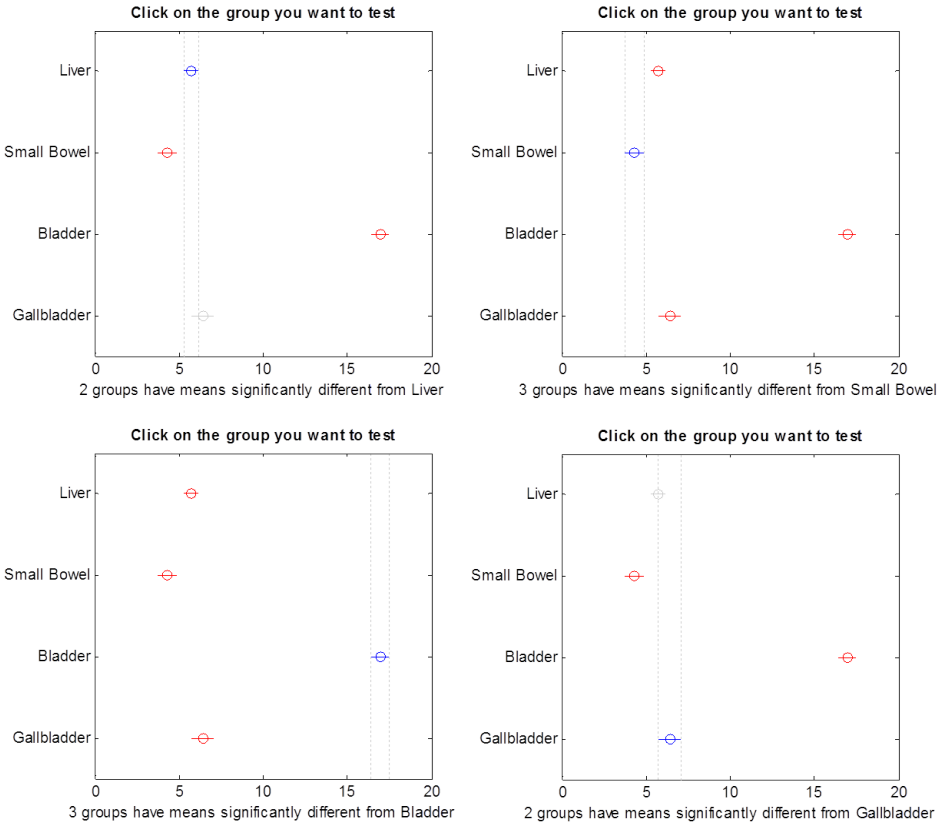

Figure 5.14: *MATLAB* multicomparison results of $\hat{\tilde{\beta}}$

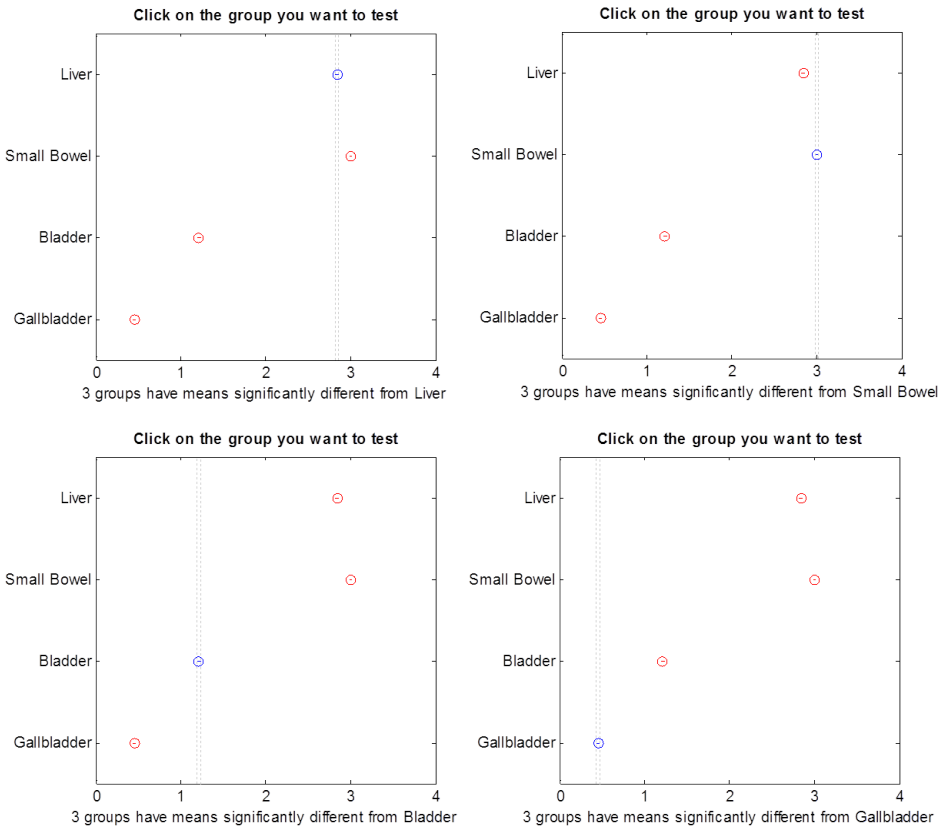

Figure 5.15: *MATLAB* multicomparison results of $\hat{d}$

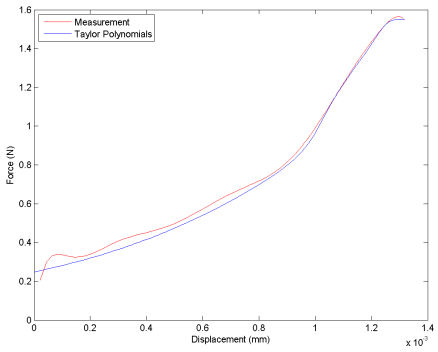

Figure 5.16: Plots of the actual and estimated force-displacement curve for 0.25Hz, 2V (1.55N) single grasp on liver tissue

Chapter 6

Conclusion and Future Work

6.1 Conclusion

In this work, we are able to characterize and quantify the force delivered to the tissue at the grasper jaws. We implemented strain gages as a force sensor at the handle and obtained the force at the grasper jaws using a nonlinear transfer function that depends on jaw angle at every instant of time. We found that the resulting force at the grasper jaws are smaller than the force applied at the handle for all jaw angles. Although the transfer function is able to map handle force to jaw force, it neglects the contribution from friction and slop within the mechanism. In order to accurately measure the force at the grasper jaws, we proposed an alternative low cost method by coating tissue with pressure indication microcapsules. However, this method is not possible to be implemented clinically.

We developed an extended Kalman filter (EKF) algorithm for estimating grasping force online and for identifying tissue types. In simulation, the EKF is able to estimate tissue parameters such as tissue stiffness coefficients (α and β) of four different abdominal tissue types closely to some reference values experimentally determined *in vivo* and *in situ* from [4]. Furthermore, the resulting tissue stress-strain behavior using the estimated paramters coincide with that of the reference. In the application, to identify tissue types of an unknown tissue being grasped, multiple EKF with various initial guess tissues could be run simultaneously, and the EKF that has fastest convergence time and smallest absolute error can be used to denote the correct tissue type being

grasped.

We modified and developed the *Smart Tool* to be an "automated tissue identifying" laparoscopic grasper capable of measuring force and displacement at the tissue. Then, we implemented the EKF algorithm for data collected from *in situ* abdominal tissues of two porcine models using the developed *Smart Tool*. The results of the EKF implementation are deemed satisfactory. The estimated tissue stiffness and damping coefficients are distinct for all four tissue types analyzed, allowing online tissue differentiation / identification. It is found from the EKF analysis that by using a grasping rate of 0.25Hz (applied force at the handle starts from 0N and reaches its maximum value within 1s), we are able to estimate the force delivered to the tissue accurately within 15% error bounds from the measured force values.

The EKF algorithm showed favorable performance in simulation, estimating delivered force within 15% error in 0.35s on average. In *in vivo* and *in situ* trials, the speed of convergence was slightly better (0.28s in average) using initial estimates of states that are close to the actual values unique to tissue typed being analyzed. However, if initial estimates are not unique to the tissue type, the convergence rate was not consistent among tissues.

We thus conclude that while the EKF algorithm works sufficiently well in estimating grasping force *in vivo*, it may not be the ideal method to support real-time tissue discrimination using only force and displacement measurement information given its sensitivity to initial estimates.

6.2 Future Work

Existing work in this thesis can be extended to include the following:

- Implement a force sensor at the grasper jaws to directly measure force delivered to the tissue at the grasper jaws. By applying a force sensor at the grasper jaws, nonlinear dependence on friction and slop can be eliminated, resulting in a more accurate measurement of force at tissue.

- Implement an elastic sensor at the grasper jaws to help estimate nonlinear parameters directly.

- The data collection could be extended to more porcine models to observe for possibility of pig-to-pig variation on tissue characteristics. Also, alternative grasping profiles should be explored.
- Apply an alternative online estimation method such as an unscented Kalman filter or a particle filter.
- Develop a control algorithm that regulates the amount of force delivered to the tissue regardless of the force applied at the grasper handle. The control algorithm will take in information of tissue type identified by the EKF.

References

[1] M. MacFarlane, J. Rosen, B. Hannaford, C. Pellegrini, and M. Mika Sinanan, "Force-Feedback Grasper Helps Restore Sense of Touch in Minimally Invasive Surgery," *Journal of Gastrointestinal Surgery*, vol. 3, no. 3, pp. 278–285, 1999.

[2] J. D. Brown, J. Rosen, Y. S. Kim, L. Chang, M. N. Sinanan, and B. Hannaford, "In-vivo and In-situ Compressive Properties of Porcine Abdominal Soft Tissues," *Studies in Health Technology and Informatics*, pp. 26–32, 2003.

[3] G. Tholey, J. P. Desai, and A. E. Castellanos, "Force Feedback Plays a Significant Role in Minimally Invasive Surgery: Results and Analysis," *Annals of surgery*, vol. 241, no. 1, p. 102, 2005.

[4] J. Rosen, J. D. Brown, S. De, M. Sinanan, and B. Hannaford, "Biomechanical Properties of Abdominal Organs In Vivo and Postmortem Under Compression Loads," *Journal of biomechanical engineering*, vol. 130, pp. 021020–1, 2008.

[5] S. De, J. Rosen, A. Dagan, B. Hannaford, P. Swanson, and M. Sinanan, "Assessment of Tissue Damage due to Mechanical Stresses," *The International Journal of Robotics Research*, vol. 26, no. 11-12, pp. 1159–1171, 2007.

[6] P. R. Roan, *An Instrumented Surgical Tool for Local Ischemia Detection.* PhD thesis, Department of Electrical Engineering, University of Washington, 2011. Copyright ProQuest, UMI Dissertations Publishing 2011.

[7] H. Xin, J. Zelek, and H. Carnahan, "Laparoscopic Surgery, Perceptual Limitations and Force: A Review," in *First Canadian Student Conference on Biomedical Computing, Kingston, Ontario, Canada*, vol. 144, 2006.

[8] J. L. Flowers, R. W. Bailey, W. A. Scovill, and K. A. Zucker, "The Baltimore Experience with Laparoscopic Management of Acute Cholecystitis," *The American Journal of Surgery*, vol. 161, no. 3, pp. 388–392, 1991.

[9] K. A. Zucker, R. W. Bailey, T. R. Gadacz, and A. L. Imbembo, "Laparoscopic Guided Cholecystectomy," *The American Journal of Surgery*, vol. 161, no. 1, pp. 36–44, 1991.

[10] A. Cuschieri, J. Hunter, B. Wolfe, L. Swanstrom, and W. Hutson, "Multicenter Prospective Evaluation of Laparoscopic Antireflux Surgery," *Surgical endoscopy*, vol. 7, no. 6, pp. 505–510, 1993.

[11] S. De, *The Grasper-Tissue Interface in Minimally Invasive Surgery: Stress and Acute Indicators of Injury.* PhD thesis, Department of Bioengineering, University of Washington, June 2008.

[12] J. Kalff, W. Schraut, R. Simmons, and A. Bauer, "Surgical Manipulation of the Gut Elicits an Intestinal Muscularis Inflammatory Response Resulting in Postsurgical Ileus.," *Annals of surgery*, vol. 228, no. 5, p. 652, 1998.

[13] J. Kalff, T. Carlos, W. Schraut, T. Billiar, R. Simmons, and A. Bauer, "Surgically Induced Leukocytic Infiltrates within the Rat Intestinal Muscularis Mediate Postoperative Ileus," *Gastroenterology*, vol. 117, no. 2, pp. 378–387, 1999.

[14] R. Anup and K. Balasubramanian, "Surgical Stress and the Gastrointestinal Tract," *Journal of Surgical Research*, vol. 92, no. 2, pp. 291–300, 2000.

[15] E. Heijnsdijk, J. Dankelman, and D. Gouma, "Effectiveness of Grasping and Duration of Clamping Using Laparoscopic Graspers," *Surgical endoscopy*, vol. 16, no. 9, pp. 1329–1331, 2002.

[16] D. Marucci, A. Shakeshaft, J. Cartmill, M. Cox, S. Adams, and C. Martin, "Grasper Trauma During Laparoscopic Cholecystectomy," *Australian and New Zealand Journal of Surgery*, vol. 70, no. 8, pp. 578–581, 2000.

[17] D. R. Fletcher, M. S. Hobbs, P. Tan, L. J. Valinsky, R. L. Hockey, T. J. Pikora, M. W. Knuiman, H. J. Sheiner, and A. Edis, "Complications of Cholecystectomy:

Risks of the Laparoscopic Approach and Protective Effects of Operative Cholangiography: A Population-Based Study.," *Annals of surgery*, vol. 229, no. 4, p. 449, 1999.

[18] J. Peters, G. Fried, L. Swanstrom, N. Soper, L. Sillin, B. Schirmer, K. Hoffman, S. F. Committee, *et al.*, "Development and Validation of a Comprehensive Program of Education and Assessment of the Basic Fundamentals of Laparoscopic Surgery," *Surgery*, vol. 135, no. 1, pp. 21–27, 2004.

[19] M. Hayter, Z. Friedman, M. Bould, J. Hanlon, R. Katznelson, B. Borges, and V. Naik, "Validation of the Imperial College Surgical Assessment Device (icsad) for Labour Epidural Placement," *Canadian Journal of Anesthesia/Journal canadien d'anesthésie*, vol. 56, no. 6, pp. 419–426, 2009.

[20] A. Macmillan and A. Cuschieri, "Assessment of Innate Ability and Skills for Endoscopic Manipulations by the Advanced Dundee Endoscopic Psychomotor Tester: Predictive and Concurrent Validity," *The American journal of surgery*, vol. 177, no. 3, pp. 274–277, 1999.

[21] J. Christian, "Atraumatic Grasping Device for Laparoscopic Surgery," November 1993. US Patent 5,258,005.

[22] T. Frank and A. Cuschieri, "Prehensile Atraumatic Grasper with Intuitive Ergonomics," *Surgical Endoscopy*, vol. 11, no. 10, pp. 1036–1039, 1997.

[23] D. Sugarbaker, A. Levine, N. Warner, E. May, and L. Crainich, "Tissue Grasping Device," July 1999. US Patent 5,928,264.

[24] R. D. Adams and S. E. Thompson, "Atraumatic Endoscopic Apparatus," February 2000.

[25] H. De Guillebon and G. Omari, "Super Atraumatic Grasper Apparatus," February 2007. US Patent 7,182,775.

[26] G. Maxymiv and M. Gustafson, "Suction Dome for Atraumatically Grasping or Manipulating Tissue," April 2007. US Patent App. 12/296,944.

[27] G. Fischer, T. Akinbiyi, S. Saha, J. Zand, M. Talamini, M. Marohn, and R. Taylor, "Ischemia and Force Sensing Surgical Instruments for Augmenting Available Surgeon Information," in *The First IEEE/RAS-EMBS International Conference on Biomedical Robotics and Biomechatronics BioRob 2006*, pp. 1030–1035, IEEE, 2006.

[28] G. Fischer, J. Zand, M. Talamini, M. Marohn, T. Akinbiyi, K. Kanev, J. Kuo, P. Kazanzides, and R. Taylor, "Intra-operative Ischemia Sensing Surgical Instruments," *Complex Medical Engineering*, 2005.

[29] M. Patkin, "Measuring Gentleness in Surgery," 2006.

[30] B. Ristic, S. Kun, and R. Peura, "Development of an Impedance Spectrometer for Tissue Ischemia Monitoring: Application of Synchronous Sampling Principle," in *Proceedings of the 1995 IEEE 21st Annual Northeast Bioengineering Conference*, pp. 74–75, IEEE, 1995.

[31] J. Rosen, B. Hannaford, M. MacFarlane, and M. Sinanan, "Force Controlled and Teleoperated Endoscopic Grasper for Minimally Invasive Surgery - Experimental Performance Evaluation," *IEEE Transactions on Biomedical Engineering*, vol. 46, no. 10, pp. 1212–1221, 1999.

[32] J. Brown, J. Rosen, M. Moreyra, M. Sinanan, and B. Hannaford, "Computer-controlled Motorized Endoscopic Grasper for In Vivo Measurement of Soft Tissue Biomechanical Characteristics," *Studies in Health Technology and Informatics*, pp. 71–73, 2002.

[33] H. W. Haslach Jr, "Nonlinear Viscoelastic, Thermodynamically Consistent, Models for Biological Soft Tissue," *Biomechanics and modeling in mechanobiology*, vol. 3, no. 3, pp. 172–189, 2005.

[34] F. B. de Casson and C. Laugier, "Modeling the Dynamics of a Human Liver for a Minimally Invasive Surgery Simulator," in *Medical Image Computing and Computer-Assisted Intervention–MICCAI99*, pp. 1156–1165, Springer, 1999.

[35] E. Turgay, S. Salcudean, and R. Rohling, "Identifying the Mechanical Properties of Tissue by Ultrasound Strain Imaging," *Ultrasound in medicine & biology*, vol. 32, no. 2, pp. 221–235, 2006.

[36] L. S. Taylor, A. L. Lerner, D. J. Rubens, and K. J. Parker, "A Kelvin-Voigt Fractional Derivative Model for Viscoelastic Characterization of Liver Tissue," in *ASME International Mechanical Engineering Congress and Exposition, New Orleans, Louisiana*, 2002.

[37] T. Yamamoto, M. Bernhardt, A. Peer, M. Buss, and A. M. Okamura, "Techniques for Environment Parameter Estimation during Telemanipulation," in *Biomedical Robotics and Biomechatronics, 2008. BioRob 2008. 2nd IEEE RAS & EMBS International Conference on*, pp. 217–223, IEEE, 2008.

[38] A. Bicchi, G. Canepa, D. De Rossi, P. Iacconi, and E. Scillingo, "A Sensor-Based Minimally Invasive Surgery Tool for Detecting Tissue Elastic Properties," in *IEEE International Conference on Robotics and Automation, 1996. Proceedings., 1996*, vol. 1, pp. 884–888, IEEE, 1996.

[39] D. P. Noonan, H. Liu, Y. H. Zweiri, K. A. Althoefer, and L. D. Seneviratne, "A Dual-Function Wheeled Probe for Tissue Viscoelastic Property Identification During Minimally Invasive Surgery," in *Robotics and Automation, 2007 IEEE International Conference on*, pp. 2629–2634, IEEE, 2007.

[40] K. Hunt and F. Crossley, "Coefficient of Restitution Interpreted as Damping in Vibroimpact," *J. Appl. Mech.*, 1975.

[41] A. Achhammer, C. Weber, A. Peer, and M. Buss, "Improvement of Model-Mediated Teleoperation sing a New Hybrid Environment Estimation Technique," in *Robotics and Automation (ICRA), 2010 IEEE International Conference on*, pp. 5358–5363, IEEE, 2010.

[42] T. Yamamoto, B. Vagvolgyi, K. Balaji, L. L. Whitcomb, and A. M. Okamura, "Tissue Property Estimation and Graphical Display for Teleoperated Robot-Assisted Surgery," in *IEEE International Conference on Robotics and Automation, 2009. ICRA'09.*, pp. 4239–4245, IEEE, 2009.

[43] X. Yu, H. J. Chizeck, and B. Hannaford, "Comparison of Transient Performance in the Control of Soft Tissue Grasping," in *IEEE/RSJ International Conference on Intelligent Robots and Systems, 2007. IROS 2007.*, pp. 1809–1814, IEEE, 2007.

[44] S. Misra and A. M. Okamura, "Environment Parameter Estimation during Bilateral Telemanipulation," in *Haptic Interfaces for Virtual Environment and Teleoperator Systems, 2006 14th Symposium on*, pp. 301–307, IEEE, 2006.

[45] F. Mobasser and K. Hashtrudi-Zaad, "Predictive Teleoperation using Laser Rangefinder," in *Electrical and Computer Engineering, 2006. CCECE'06. Canadian Conference on*, pp. 1279–1282, IEEE, 2006.

[46] G. De Gersem, *Kinaesthetic Feedback and Enhanced Sensitivity in Robotic Endoscopic Telesurgery*. PhD thesis, 2005.

[47] T. Hoshi, Y. Kobayashi, and M. Fujie, "Developing a System to Identify the Material Parameters of an Organ Model for Surgical Robot Control," in *Biomedical Robotics and Biomechatronics, 2008. BioRob 2008. 2nd IEEE RAS & EMBS International Conference on*, pp. 730–735, IEEE, 2008.

[48] A. Sie and T. M. Kowalewski, "Quantifying Forces at the Tool-Tissue Interface of a Surgical Laparoscopic Grasper," *Journal of Medical Devices*, 2013.

[49] A. Sie, M. Winek, T. M. Kowalewski, *et al.*, "Low-Cost Quantitative Tool-Tissue Applied Pressure Indication Method for Surgical Training and Assessment in Reality-Based Physical Models.," *Studies in health technology and informatics*, vol. 184, pp. 407–411, 2012.

[50] T. M. Kowalewski, *Real-time Quantitative Assessment of Surgical Skill*. PhD thesis, University of Washington, 2012.

[51] R. E. Kalman, "A New Approach to Linear Filtering and Prediction Problems," *Journal of Basic Engineering*, vol. 82, no. 1, pp. 35–45, 1960.

[52] P. Holoborodko, "Smooth Noise Robust Differentiators." http://www.holoborodko.com/pavel/numerical-methods/numerical-derivative/smooth-low-noise-differentiators/, 2008.

Appendix A

Glossary and Acronyms

Care has been taken in this thesis to minimize the use of jargon and acronyms, but this cannot always be achieved. This appendix defines jargon terms in a glossary, and contains a table of acronyms and their meaning.

A.1 Glossary

- **Distal End** – Section of a surgical tool that is furthest away from the body of the operator. For the case of the laparoscopic grasper discussed in this work, distal end is the grasper jaws.
- **Haptic Feedback** – Force based feedback from interaction between the hand or arm to an object.
- **Proximal End** – Section of a surgical tool that is closest from the body of the operator. For the case of the laparoscopic grasper discussed in this work, proximal end is the handle.
- ***Smart Tool*** – Smart instrumented laparoscopic surgical grasper developed in this work based on the *MSEG* developed in [6].
- **Tactile Feedback** – Touch or palpation based feedback from interaction between the hand to an object.

A.2 Acronyms

Table A.1: Acronyms

Acronym	Meaning
ADEPT	Advanced Dundee Endoscopic Psychomotor Tester
EKF	Extended Kalman Filter
FLS	Fundamentals of Laparoscopic Surgery
FREG	Force Feedback Endoscopic Grasper
GUI	Graphical User Interface
ICSAD	Imperial College Surgical Assessment Device
MEG	Motorized Endoscopic Grasper
MIS	Minimally Invasive Surgery
MSEG	Motorized Smart Endoscopic Grasper
RLS	Recursive Least Squares

A.3 *LabVIEW* Block Diagram of *Smart Tool* GUI

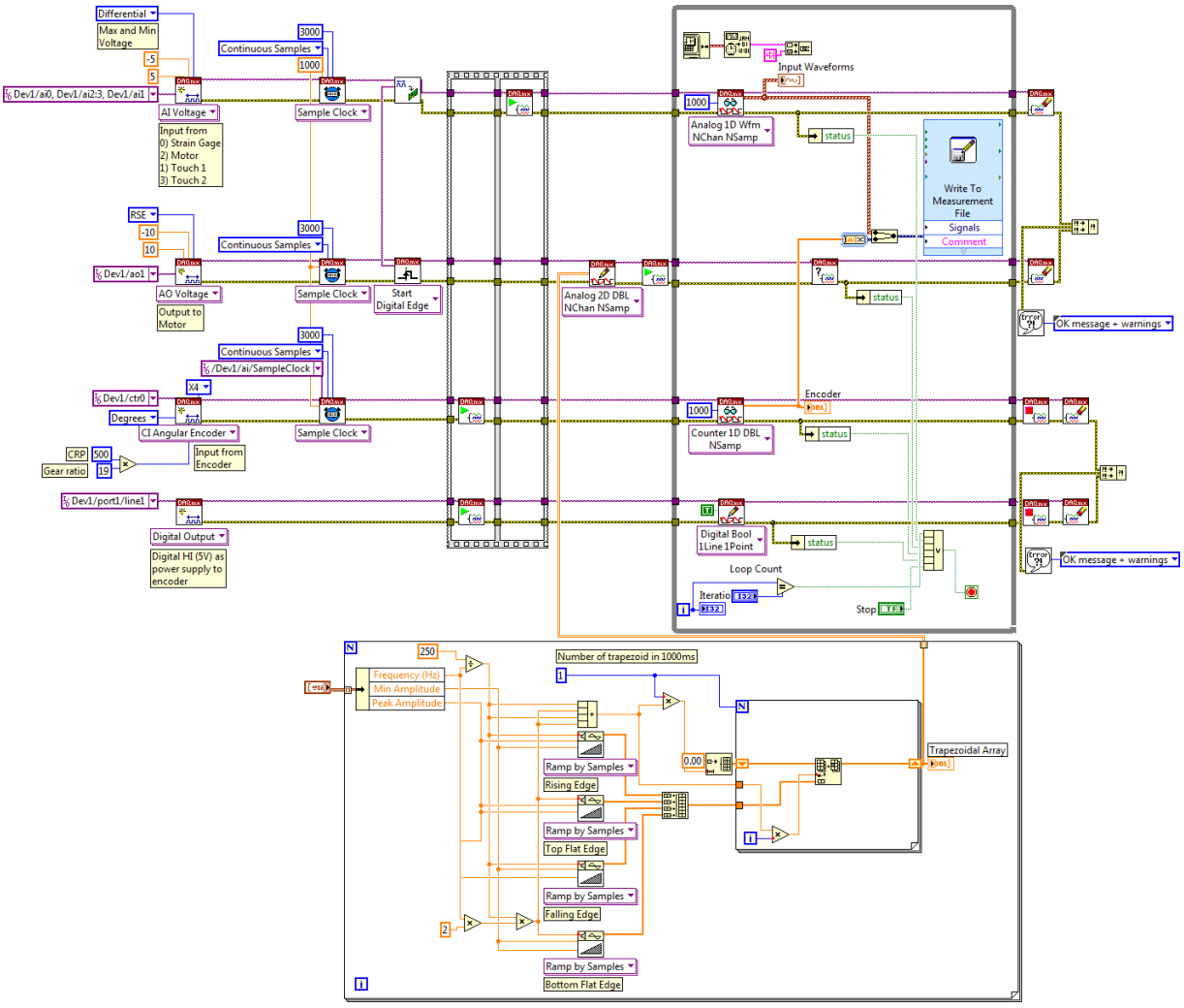

Figure A.1: Block diagram of *Smart Tool* GUI in *LabVIEW*